
Unterschrift BetreuerIn



BACHELORARBEIT

**Software implementation of the quality
assurance tool for magnetic resonance imaging
distortion assessment**

Betreuer:

*Ao. Univ. Prof. Dipl.-Ing. Dr.techn. Martin Gröschl
Institut für Angewandte Physik
Technische Universität Wien*

in Kooperation mit:

*Peter Kuess, PhD
& Piotr Andrzejewski, MSc Eng
Department of Radiooncology
Medical University Vienna, AKH Vienna*

von:

David Blacher
1327545

Technische Physik
E033261

July 24, 2017

Unterschrift StudentIn

Kurzzusammenfassung

deutsch?

Abstract

english

Contents

1	Introduction	1
1.1	Photon - matter interactions	1
1.2	Radiobiology	3
1.2.1	The human cell	3
1.2.2	Effects of radiation	4
1.3	Imaging modalities	5
1.3.1	X-ray projection imaging	5
1.3.2	Computer Tomography - CT	6
1.3.3	Magnetic Resonance Imaging - MRI	11
1.3.4	Non morphologic Imaging	13
1.4	External Beam Radiation Therapy	16
1.4.1	Role of CT	18
1.4.2	Role of MRI	19
1.5	Aim of this work	19
2	Material and methods	21
2.1	Scanners	21
2.1.1	MRI scanner - field distribution	21
2.2	Custom build phantom	26
2.2.1	Frame and rods	26
2.2.2	Rod fillings	28
2.3	Sequences	30
2.4	Developed software tool	30
2.4.1	Processing MRI and CT scans	31
2.4.2	Capabilities	34
2.4.3	Measuring distortion	34
2.4.4	Calculation: dice-coefficient (DC)	35
2.4.5	Calculation: center of mass (COM)	35

3 Results	39
3.1 Obtained MRI and CT scans	39
3.2 Tested solutions	42
3.2.1 Visibility on CT/MRI scans	42
3.2.2 Mechanical properties of solutions	43
3.3 Distortion assessment	45
3.3.1 Distortion	45
3.3.2 DC	48
4 Discussion	53
4.1 Phantom design	53
4.1.1 observed issues	53
4.2 Tested solutions	54
4.2.1 Thoughts about choosing possible candidates	54
4.2.2 Choosing a promising candidate	56
4.3 Sequence	57
4.4 Distortion	57
5 Conclusion and Outlook	59
5.1 Liquid for phantom	59
5.2 Future improvement of software tool	59
Bibliography	61

1 Introduction

1.1 Photon - matter interactions

As light passes through matter, its intensity decreases. This phenomenon is due to photons interacting with electrons, nuclei, and their electric fields. All processes either change the direction they travel in, alter their energy, or result in the disappearance of single photons. The probability of these interactions differ for each material (dependent on its density; proton number Z) and photon energy ($h\nu$).

If a photon's energy exceeds the binding energy of an orbital electron, the **photo-electric interaction** can occur. Also known as 'photo effect', it describes a photon being completely absorbed by a tightly bound orbital electron which then is ejected from its atom. The now free electron is called 'photo-electron'. Its kinetic energy is the difference of the photon's energy and the electron's binding energy:

$$E_{kin} = h\nu - E_{binding} \quad (1.1)$$

Instead of being absorbed, photons might also just 'bounce off' electrons or entire atoms, transferring momentum and, in some cases, part of their energy to the particle they collide with. **Rayleigh (coherent) scattering** happens when a photon interacts with a tightly bound orbital electron (transferring momentum to the entire atom). This event can be seen as elastic, because only a negligible part of the photon's energy is transferred.

The **Compton effect (incoherent scattering)** involves a essentially free electron, such as an orbital electron with a relatively small binding energy compared to the photon's energy. Due to the weak binding, momentum is transferred only to the electron. This 'recoil electron' (or 'Compton electron') leaves its atom with a significant kinetic

energy, which originated from the scattered photon. Since the photon loses part of its energy, the event is considered inelastic.

When a photon with an energy above 1.02 MeV passes through the electric field of a nucleus, it might disappear to create an electron-positron pair. This effect is called **pair production**. The threshold of 1.02 MeV equals exactly the rest mass $E_m = 2m_e c^2$ for the two equally heavy particles. The new particles travel in opposite directions with the same kinetic energy:

$$E_{kin} = \frac{h\nu - 1.02 \text{ MeV}}{2} \quad (1.2)$$

A photon with energy of the order of 2 MeV or higher can also interact directly with the nucleus. Such a **Photonuclear reaction** is similar to the photo effect, in the sense that the photon is completely absorbed. Its energy is transferred to the nucleus resulting in the emission of either a proton or neutron. [41, 27]

Attenuation

The aforementioned interactions result in a gradual decrease of light intensity as it travels through matter. The combined effect is described by **Beer's law**:

$$I(x) = I_0 e^{-\mu(h\nu, Z)x} \quad (1.3)$$

where x is the thickness of a homogeneous material and μ its linear attenuation coefficient. The different probabilities for the interactions to occur is implicitly considered by the attenuation coefficient $\mu(h\nu, Z)$ (see Figure ?? and 1.1).

For a photon being transmitted through matter with varying properties, the attenuation coefficient changes, too. After travelling a distance d , the intensity can be expressed as:

$$I(x) = I_0 e^{- \int_0^x \mu(x) dx} \quad (1.4)$$

Where $\mu(x)$ describes the attenuation at every distance x .

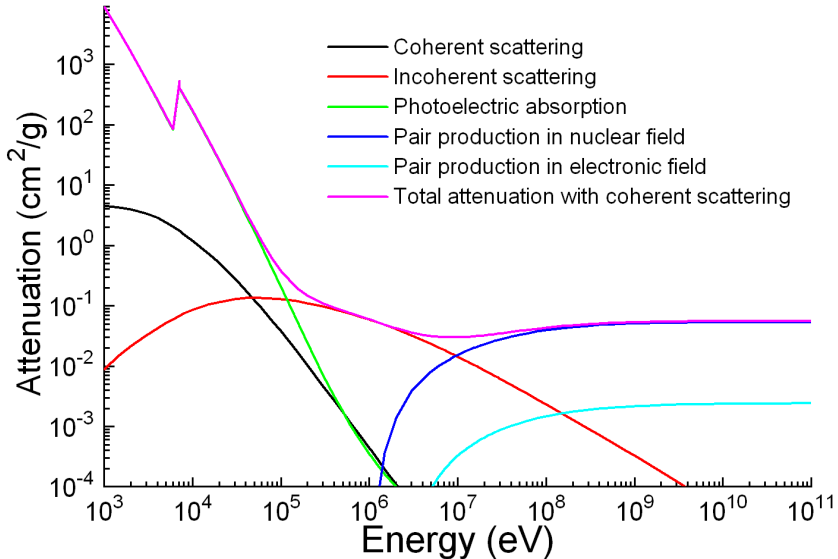


Figure 1.1: Photon attenuation for iron; [Materialsscientist]

1.2 Radiobiology

(TODO: better name for chapter! maybe more general?)

1.2.1 The human cell

All living creatures consist of cells working together to form what is called tissue. A collection of tissues which perform one or more functions is considered an organ.

Even though different types of cells exhibit distinctive traits which set them apart, all of them originated from the same totipotent zygote containing a original set of DNA. A zygote is a stem cell, it has the ability to replicate indefinitely, passing its DNA on to the resulting daughter cells. At the same time, it can change into any type of body cell. This feature is why it is called 'totipotent'. As soon as the zygote has divided into a sufficient

number of identical cells, all of them differentiate into the various human tissues. In favour of becoming more specialised cells, they lose their totipotency. During the early stages of an embryo they are still capable of developing into a number of different cell types, but already restricted to their own tissue type; either nerve, skin, or blood & muscle tissue. As those cells further specialise, they limit their potential even more. In a fully grown human body there are still stem cells present, such as bone marrow stem cells. Other than the zygote, bone marrow can only give rise to blood cells, but not to e.g. nerve or skin cells. A blood cell itself cannot replicate, it is considered a 'mature cell'.

The whole process follows guidelines dictated by the DNA. Every cell inherited its own personal copy of the original set. Inevitably, mistakes happen during its replication resulting in changes to the DNA called 'mutation'. Most of these alterations are repaired or do not lead to changes in the cells behaviour. As the human body ages, the repair mechanism slows down and mutations accumulate. At one point, a cell is reprogrammed to act in a unpredictable way, giving up its duties and duplicating without restraint, forming tumours. External factors are known to influence cell behaviour and induce such 'malign' cells (carcinogenesis). Cancer cells usually replicate more frequent than healthy cells, eventually leading to characteristic symptoms.

Different approaches have been developed to treat cancer, not all of which are suited to tackle every type of tumour. If the tumour's location is unknown or metastases have formed already in many places, chemotherapy might be considered. An easily accessible tumour could be removed in a surgery. Non invasive therapies also include radiotherapy, destroying cancer cells using radiation.

Generally, early treatments have high chances of success, but tumours are often not noticed until they reached a certain stage. Reliable ways of diagnosing tumours are made possible by imaging techniques visualising the interior of the human body. **[Baumann2017]**

1.2.2 Effects of radiation

As described in 1.1, light transfers some of its energy to the medium it passes through. Most interactions, such as the photo effect, incoherent (Compton) scattering, and pair production, result in free electrons. If the electron has a sufficiently high kinetic energy, it may free additional orbital electrons from atoms in its vicinity. The remaining ions are then left positively charged, with a single unpaired valence electron. This type of

chemical and free electrons are called 'radicals' and considered extremely reactive. They are likely to take part in chemical events which lead to the breakage of chemical bonds. Such processes can induce changes in DNA sequences and eventually produce biological damage.

A irradiated cell can be affected in various ways ranging from no effect to cell death. The cell might survive containing a minor mutation. A more fundamental mutation might lead to carcinogenesis. Irradiated cells might also send signals to their neighbours, inducing genetic damage known as 'bystander effects'. However, surviving cells can also react to irradiation and becoming more resistant.

Changes to the DNA might not become apparent ever, others take years until they result in biological effects. A well known long term consequence of ionising radiation is leukaemia. Damage to germ cells (sperm/egg) might even result in genetic damages expressed in subsequent generations.

While imaging modalities utilising x-rays are designed to apply a dose as little as possible to keep effects of irradiation low, radiotherapy makes use of the lethal effects targeting cancer cells. [41, 27]

1.3 Imaging modalities

1.3.1 X-ray projection imaging

A widely used imaging technique based on photon interactions is X-ray projection. Its setup is made up by a light source, the object of interest, and a detector. Since the technique is about projection, a patient needs to be placed between an X-ray tube and the detector (usually a film-cassette or digital sensor). In the first stage of the imaging process, X-ray photons emitted by the tube enter the body. Next, while travelling through human tissue, they interact with its atoms in various ways (see 1.1). These processes govern how much radiation is absorbed or scattered. Finally, Photons which make it through the patient are recorded as they reach the detector on the opposite side. This results in a negative greyscale image, where brightness values correspond to the intensity reduction. Low intensity (= high absorption) leads to bright spots on the image and vice-versa. The whole process could also be described as 'the projection of attenuation shadows on to the detector', since the radiation absorption directly depends on the attenuation coefficient. The attenuation, on the other hand, depend on the

tissue's properties (e.g. proton number Z , density, etc). Consequently, the attenuation shadows depict inner structures of the patient.

Soft tissue contrast

Soft tissue such as brain matter and muscles absorb only little radiation, casting a lighter shadow (dark areas on image) than bone which absorbs more photons (bright areas). Anything other than bone differs only slightly in attenuation, owing to the relatively small difference in atomic numbers and density. For this reason, X-ray projection imaging is considered reliable when it comes to diagnose bone fractures, while at the same time, it is not suited to clearly delineate soft tissue structures.

Other imaging modalities are better suited for the latter, like medical ultrasound and Magnetic Resonance Imaging (MRI), to name a few. They are preferred for non invasive soft tissue examinations. If these imaging modalities are no option, X-ray projection can still be of some use in combination with contrast agents. Such substances fill e.g. the bloodstream with heavier atoms, which can be clearly seen against the dark background of surrounding soft-tissue. In CT angiography, for instance, iodine is administered intravenously enhancing vessel to vessel-wall contrast. In studies of the abdomen a diluted iodine solution or barium compounds swallowed by the patient leads to improved visibility of the gastrointestinal tract.

For patients allergic to those chemicals, a number of alternative agents have been developed. Unfortunately most introduce slight, sometimes serious side-effects. There is ongoing research to find materials yielding enhanced contrast while at the same time minimising adverse reactions, a promising candidate being gold nano particles. [41, 27]

1.3.2 Computer Tomography - CT

(TODO: The most important thing about CT is that it is super fast and that it does not introduce distortions. The disadvantages are the radiation dose and low soft tissue contrast)

Computer Tomography (CT) is a three-dimensional (3-D) imaging modality based on the measurement of X-ray attenuation. The technique has evolved from 2-D X-ray scanning. By mounting source and detector on a rotary ring with a patient at the centre, projections from any angle can be obtained. However, in contrast to 2-D projection methods, the detector resembles an arc made up by 800 to 900 neighbouring detector

elements. A single 'image' taken by the detector is therefore only in 1-D. Yet, by repeating this process from a sufficient number of different angles and along the entire patient (z-axis) a 3-D model can be computed. In contrast to 2-D methods, where the patients interior is projected/compressed onto a flat image, CT preserves the exact location information. This feature led to a radical improvement in diagnostics.

Since its clinical introduction in 1971, CT has become a widely used 3-D imaging modality for a range of applications including radiation oncology. Especially in radiation therapy, knowledge of the exact geometry is crucial, which is why CT plays such an important role in treatment planning (see 1.4). [41, 27]

3-D image reconstruction

As a photon passes through the patient, it encounters different materials associated with characteristic linear attenuation coefficients. It is practical to think of the scanned body as a collection of $N = N_X \cdot N_Y \cdot N_Z$ finite size cubes (Δx cube length) called 'voxels' (analogous to pixels in a 2-D digital photograph). The entire model can then be regarded as a 3-D matrix, with the attenuation coefficients μ_i of the voxels as its entries. Figure 1.2 represents a (4, 4, 1) matrix. It depicts the path an X-ray may follow passing through voxels with different values μ_i . This discretisation allows us to change equation 1.4 to:

$$I(x) = I_0 e^{-\sum_{i=1}^{N_X} \mu_i \Delta x} \quad (1.5)$$

The initial and final intensities can be read of the settings of the X-ray tube and the detected signal. Based on these values, image reconstruction algorithms derive the three-dimensional linear attenuation coefficient matrix. For convenience, the computed numbers are converted to Hounsfield Units which are displayed in the final image. [41, 27]

Hounsfield Units

In a final CT scan, voxel values are recorded in Hounsfield Units (HU), which relate to the attenuation of water at room temperature:

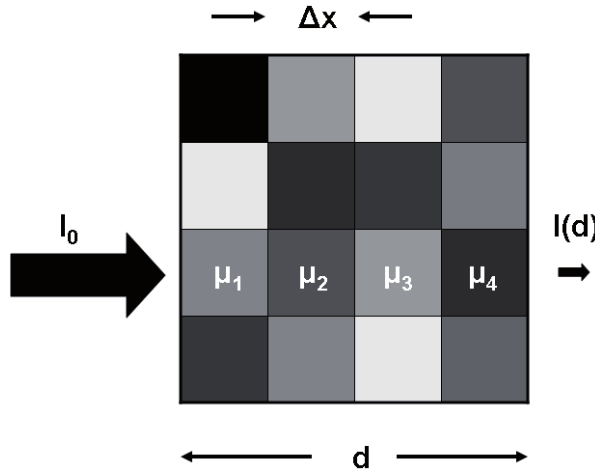


Figure 1.2: Simplified attenuation matrix (4,4,1); [27]

Table 1.1: Average HU values for various types of human tissue

Substance	HU
Air	-1000
Lung	-750 (-950 to -600)
Fat	-90 (-100 to -80)
Water	0
Muscle	+25 (+10 to +40)
Brain, white matter	+25 (+20 to +30)
Kidneys	+30 (+20 to +40)
Brain, grey matter	+35 (+30 to +40)
Blood	+55 (+50 to +60)
Liver	+60 (+50 to +70)
Compact bone	+1000 (+300 to +2500)

$$HU_{material} = \frac{\mu_{material} - \mu_{water}}{\mu_{water}} \cdot 1000 \quad (1.6)$$

Table 1.1 lists types of human tissue and their values on the HU scale. Generally, HU values range from -1024 to +3071 (12 bit), but the upper limit can be extended to 15,359 (14 bit) if materials with even higher attenuation need to be visualised (e.g. implants).

Typically, CT scans are displayed on Computer monitors, which imposes the need to map the HU values to a 8-bit greyscale (256 steps of luminosity). Since the number of

possible values (dynamic range) on the HU scale is 16 times the shades of grey on a screen ($12-8 = 4$ bit difference; equivalent to a factor of 2^4) the screen cannot convey all details at the same time. A linear mapping would result in 16 neighbouring HU values being compressed to the same brightness on the screen. This way, the brightest (bone) and darkest parts (soft tissue) of the image would be clearly distinguishable. At the same time small differences (<16 HU) would appear as exactly the same intensity. However, most of the time, the doctor's focus might lie either on soft tissue or bone material. Bearing in mind that soft tissue values range only from 10 HU to 70 HU at most (see table 1.1), such a compression would make distinguishing tissues using CT very unreliable. Instead of showing detail from the lowest to the highest value, a range of values - a so called window - can be chosen. Let's assume, for example, a range from -100 to 155 HU to be of interest. This selected range can be mapped directly and uncompressed to a 8-bit greyscale. Any values above 155 HU will be assigned the brightest value (white = 255), below -100 the darkest (black = 0). While showing very good soft tissue contrast, all bones would be depicted with exactly the same brightness (255), even though they might have a varying HU values. For bone structures a range from 300 to 2500 HU might show sufficient contrast. Standard computer programs used to display CT images allow the user to change the window interactively to any value range. [41, 27]

Image acquisition

The time necessary to collect 1-D attenuation projections from sufficient angles is called 'acquisition time'. In 2-D X-ray scanning only one picture is taken, while a 3-D CT model is made up of a photo sequence. If the patient moves during the imaging process, the final model would show motion artefacts which might lead to wrong conclusions. Consequently, CT scanners are designed to minimise acquisition time while ensuring sufficient image quality. Very fast CT protocols result in smaller resolution, because less images are taken. It has to be said though that CT acquisition time is usually significantly shorter than MRI. [41, 27]

Image quality

Additionally to the relatively short acquisition time, CT scans show little distortion compared MRI (see 1.3.3), which is why they are often used as 'gold standards' (reference scans used for MRI calibration or distortion assessment).

While bone structures are clearly visible in CT scans, 'soft tissue contrast' is relatively low compared to MRI. In other words, parts of the body which are considered as 'soft tissue' (intestines, brain, blood vessels, etc.) differ little in brightness and are therefore hard to distinguish. See 1.3.1 for more information.

Another aspect of image quality is the 'low contrast resolution' of the scan. It directly relates to how much structures and their surroundings have to differ in signal intensity to be clearly distinguishable by doctors. The quality of the 'low contrast resolution' is mainly limited by noise. Noise is a random pattern underlying the actual signal which is always present to some extent. Its prominence in the final image is described by the Signal to Noise Ratio (SNR). If the SNR is too low, fine structures blend with the noise and cannot be distinguished. Strategies to achieve a high SNR include raising the initial photon flux (intensity) or employing contrast agents. The intensity is governed by the tube current, which is limited by the heat capacity of the tube and health considerations regarding the patient.

Alternatively, the spatial resolution can be decreased, effectively combining neighbouring image slices. This way the SNR for the combined slices is increased, but fine structures along the z-axis might be lost due to the reduced resolution. [41, 27]

Health considerations

CT scans describe the attenuation throughout a patient, which is directly related to how much energy is transferred from photons to matter. Only because x-rays are absorbed by the human body, this imaging modality gives insight in the density distribution of a body's interior. However, this transferred energy is capable of causing biological damage. (see 1.2.2)

While the radiation dose administered during a single CT scan is almost negligible, patients receiving this dose regularly end up with a potentially harmful accumulated amount of radiation. Cancer patients, for instance, need to be imaged frequently during treatment planning. On the one hand, the dose is necessary for an effective treatment / removal of the tumours. On the other hand, the long term effects of the administered dose lead to induced cancer. However, patients might die before those consequences come into effect. Therefore, it's typically children (who received a great number of CTs) to suffer from induced cancer occurring up to 40 years later. So while the benefit from using CT for diagnostics far outweighs the damage, there have been major efforts to reduce dose while maintaining reasonable image quality. [34, 5, 56, 55, 29, 16]

1.3.3 Magnetic Resonance Imaging - MRI

Magnetic Resonance Imaging (MRI) is a 3-D imaging modality based on Nuclear Magnetic Resonance (NMR), a phenomenon discovered by physicist Isidor I. Rabi in 1938. Atomic particles such as protons have an inherent quantum mechanic feature called 'spin', which is associated with a magnetic moment μ . Without an external field a proton's spin is oriented in a random direction in space and so is its magnetic moment. The sum of magnetic moments belonging to a great number of protons results in a net magnetisation. Due to their random orientation, the net magnetisation will be zero. This is because, on average, for every proton's spin there is always another particle's spin oriented exactly the opposite way, cancelling its magnetic moment.

In the case of an applied external magnetic field, the spins will either align parallel (pointing in the same direction) or anti-parallel (opposite direction) to this field, minimising their energy. Parallel protons have a lower energy than those pointing the other way. In a collection of many spins, the number of parallel spins will therefore slightly dominate, resulting in a net magnetisation greater than zero (see figure 1.3).

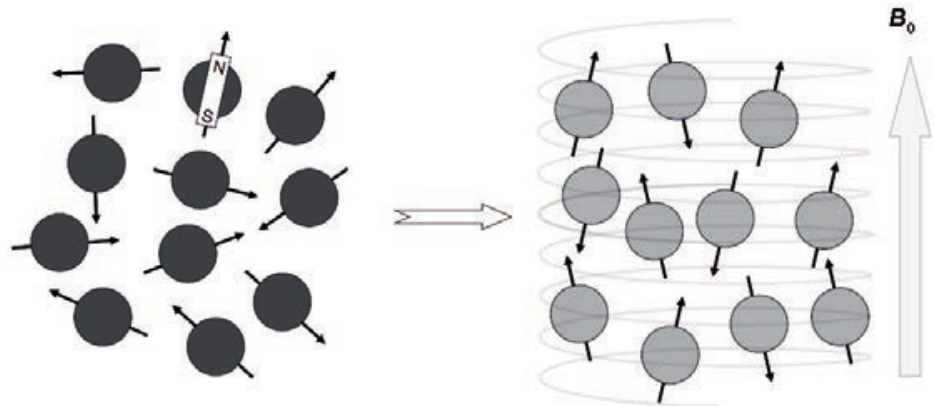


Figure 1.3: The spins, initially oriented randomly in space, become aligned either parallel or antiparallel to an externally applied magnetic field B_0 . [27]

By applying a short radio frequency pulse, the total external magnetic field changes and the magnetic moments start precessing around that new external field. The pulse duration is usually chosen as to flip the spins by a 90° angle. They are now oriented in the transverse plane to the original external field, and so is the resulting net magnetisation. Similar as to how a spinning top rotating at an angle to the direction of gravity precesses, the magnetic moments will now precess about the direction of the external field with a frequency linearly proportional to the external field strength. This preces-

sion movement can be detected as induced current in a pick-up (receiver) coil, because the net magnetisation still follows the spins' orientation. Again, the particles would like to minimise their energy by aligning their spins to the external field, but in order to do so they need to give away the additional energy, transferring it to the surrounding lattice. Those spin-lattice interactions happen with different efficiency depending on the tissue. The time it takes the spins to align is expressed in a material specific time constant T_1 . Shortly after applying the radio frequency pulse, regions of the body where magnetic moments align quickly (short T_1) have a stronger net magnetisation (in the direction of the external field) than those where energy is being transferred slowly (long T_1).

At the same time, the spins interact with each other, affecting the local magnetic field and spins in their vicinity. The magnetic moments, which started out precessing in phase directly after the radio frequency pulse flipped them, will precess at slightly different frequencies, due to the small fluctuations of the local magnetic field. The differences cause the collection of magnetic moments to 'de-phase' and the net magnetisation in the transverse plane to vanish. This process caused by spin-spin interactions is described by the material specific time constant T_2 . Eventually, all spins will be again aligned either parallel or anti-parallel to the external field, just as they were before the RF-pulse.

Applying the RF pulse with a homogeneous field strength along the whole body would excite all spins simultaneously. In order to localise differences in tissue magnetisation, the RF pulse is instead combined with a linear magnetic gradient field 'selecting' a slice to be imaged at a time. The rest of the body is unaffected, and the signal measured directly after such a pulse originates only from the chosen slice. Consequently, collecting data on the net magnetisation throughout the body in different locations ('scanning' the patient slice by slice) results in a 3-D image. As the region of interest is usually limited to a specific organ, receiver coils are available in different sizes and shapes, designed to fit the patient with a comfortable but narrow space in between.

Doctors can choose to create images that reflect the spin-lattice interactions (T_1 weighted) or the spin-spin interactions (T_2 weighted). The set of parameters governing how the tissue is excited and data acquired are called 'image sequence'. Delineating tumours or lesions is often accomplished by looking at both T_1 and T_2 weighted images and drawing the right conclusions.

Soft tissue contains a lot of water, which is made up by oxygen and hydrogen. Hydrogen nuclei are single protons and their NMR is what MRI is tuned to make visible.

This is why soft tissue appears as bright areas in MRI, whereas bone material has only little contrast. [10]

Studies have shown that delineating certain types of tumours, for example prostate cancer, is more accurate using MRI images than using CT. [46, 12, 47] Whereas in diagnostics, MRI scans might be sufficient, radio therapy treatment planning needs more/other information about the regions surrounding the tumour. MRI lacks some of those insights, which is why CT is still an essential part for external beam radiation therapy. (see 1.4)

1.3.4 Non morphologic Imaging

Diffusion Weighed imaging

Diffusion weighted (DW) imaging quantifies molecular diffusion in the body. This imaging technique uses MRI technology slightly different: Additionally to the gradients needed to select a slice (strength $3 - 5 \text{ mT/m}$, duration $2 - 4 \text{ ms}$), the sequence for DW imaging applies two long strong consecutive and opposite gradients (strength $30 - 50 \text{ mT/m}$, duration 20 ms) during which molecules may move due to diffusion. After those two gradients (which, actually, have to be applied in all three Cartesian directions), the remaining signal (net magnetisation) is measured by the receiver coil.

Molecules which are restricted in their movement will experience two equally strong but opposite magnetic fields. The first will cause them to precess with a certain speed (linear with field strength), effectively changing their phase. The second will cause them to precess exactly the other way around (same strength, but other direction), effectively returning them to their initial state. Now, they will again be in phase and result in a net magnetisation which is not zero, visible as bright areas on the scan.

Those molecules which are free to move, however, will not experience a constant field strength. As they move through the body they will precess at varying speeds during the first and then at different speeds during the second gradient. As a result, they will be out of phase when the net magnetisation is measured by the receiver coil, not causing bright areas in the scan.

DW imaging can be used to diagnose acute strokes (brain infarct), because areas with restricted diffusion (blocked blood flow) show a strong signal compared to healthy tissue with normal diffusion. Since the time necessary to allow the molecules to move during the two gradients is relatively long, the image will naturally be T_2 weighted. This is

taken into account by creating a second image which is also T_2 weighted, but does not apply two consecutive opposite gradients. The difference between the DW and the not DW weighted sequences reflects the actual contribution of diffusion (apparent diffusion coefficient - ADC).

(TODO: Perfusion?) (TODO: Spectroscopy?) (TODO: fMRI?)

Image Quality

Contrary to CT, MRI is prone to distortion, due to field inhomogeneities. For most applications, small position shifts and deformations are of minor importance. In RTTP however, those effects can have a big impact. Therefore, MRI scanners usually come equipped with an internal distortion correction algorithm. Those methods are developed by the company designing the scanners. Knowing the technical details enables them to write tailor-fit scripts which drastically reduce the distortion.

While its soft tissue contrast is superior to CT, a relatively long acquisition time is necessary to achieve a sufficient high SNR. This leads to the risk of motion artefacts (patients moving during the scanning procedure). To tackle this issue, resolution can be reduced, effectively combining signal from several voxels to create a single voxel, reducing the overall noise. The trade-off is that fine structures might get lost.

The key difference between CT and MRI considered in this work is the unavoidable distortion occurring in MRI images. Mainly caused by inhomogeneities of the magnetic fields, organs might appear shifted, elongated or shrunk. The effect is most prominent along the outer edges of the scanners field-of-view (FOW). In the isocentre (middle) of the scanner, the distortion is smaller, because here the field is least aberrant.

Health considerations

Strong static magnetic fields up to $3T$ are present around MRI scanners at all times, and precautions are necessary to ensure safety for patients and medical personnel. Ferromagnetic materials (such as steel and iron) can become dangerous projectiles in vicinity of the MRI scanner. They must be excluded from the room housing the magnet without exception. It is also important to remember that medical implants, including but not restricted to cardiac pacemakers and hearing-aids, might malfunction or become damaged in strong fields regardless whether they contain ferromagnetic materials. Patients with such implants might still be imaged with scanners utilising weak fields up to $0.5T$.

The RF pulses repeatedly put spins in excited states, transferring energy to the human body. MRI scanners are designed to limit the rise of a patient's body temperature to 0.5°C during standard imaging. Only with either medical or appropriate psychological monitoring the limit raises to 1°C . For any higher values a ethics committee approval is necessary. In general, patients should be exposed to RF fields only as strong as their thermoregulatory system is capable to cope with.

Finally, magnetic field gradients are applied together with the RF pulse. They are switched at high frequencies leading to induced currents in conducting body tissue. In principle, those currents stimulate nerves which might result in muscle twitching or pain. However, gradient levels are set to avoid stimulation. During studies some subtle biological effects have been reported, but there was no evidence pointing towards harm caused by short term exposures. At the same time, patients suffering from epilepsy might show increased sensibility to induced electric fields in the cortex. Such subjects should be imaged with caution. [27]

Open bore MRI scanners

(TODO: low fields -> less distortion??) The radiation oncology department of the Vienna General Hospital (AKH) is equipped with an $0.35T$ open-bore, c-arm MRI scanner. This open design has proven to drastically improve the well-being of patients who experience anxiety in closed-bore scanners which is why the number of incomplete MR examinations due to a claustrophobic events is low. [15, 3] Besides, patients who wouldn't fit in closed designed scanners can be imaged. Furthermore, brachytherapy patients can be placed in the scanner with applicators attached.

This scanner's field is weaker than the field of a conventional closed bore scanner (1-3 Tesla). High field strengths would result in greater resolution, better Signal to Noise (SNR) ratio, and faster imaging time. Generally, diagnostics benefit from greater image quality. However, at some point diagnostic accuracy stops increasing with field strength. At the same time astonishing improvements can be achieved at low fields. A "combination of field independent polarisation [...] with frequency optimized MRI detection coils [...] results in low-field MRI sensitivity approaching and even rivalling that of high-field MRI." [8]

Apart from the often satisfactory image quality, there are considerable cost advantages to the use of lower field MRI. The initial purchase price and the ongoing maintenance expenses are considerably lower than those of high field scanners which often use su-

perconducting magnets cooled with liquid helium. [49] Permanent magnets might be weaker, but do not require constant cooling. Low fields allow facilities to build smaller rooms and magnetic objects are less dangerous.

1.4 External Beam Radiation Therapy

External Beam Radiation Therapy (EBRT) utilizes ionizing radiation to damage cancer cells in order to stop them from multiplying. This prevents the growth of tumours and hopefully cures the patient. In conventional EBRT, photons (x-rays) in the range of 4MeV to 20MeV are used to administer the necessary dose at the location of the tumour. Unfortunately, light interacts with all cells it is passing through until it is fully absorbed. It releases its energy along its entire path while travelling through the patient. This may result in energy being transferred to cells all the way from the point of entry to the point where the (weakened) ray leaves the patient.

Charged particles (e.g. protons or carbon ions) minimise the damage done to healthy tissue due to their distinctive behaviour in energy loss called “Bragg Peak”. They release most of their energy only shortly before being stopped completely. [35] This effect can be used to spare tissue lying behind the tumour from radiation entirely and also reduce the amount of energy transferred to those lying before. [38] A comparison between the behaviour of x-rays and protons is shown in figure 1.4.

While travelling through matter both types of radiation release energy mostly due to coulomb interactions with the outer shell electrons of atoms. Knowing the electron density of the targeted tissue area is therefore essential. In order to reach a specific penetration depth, the particles' initial energy has to be chosen accordingly.

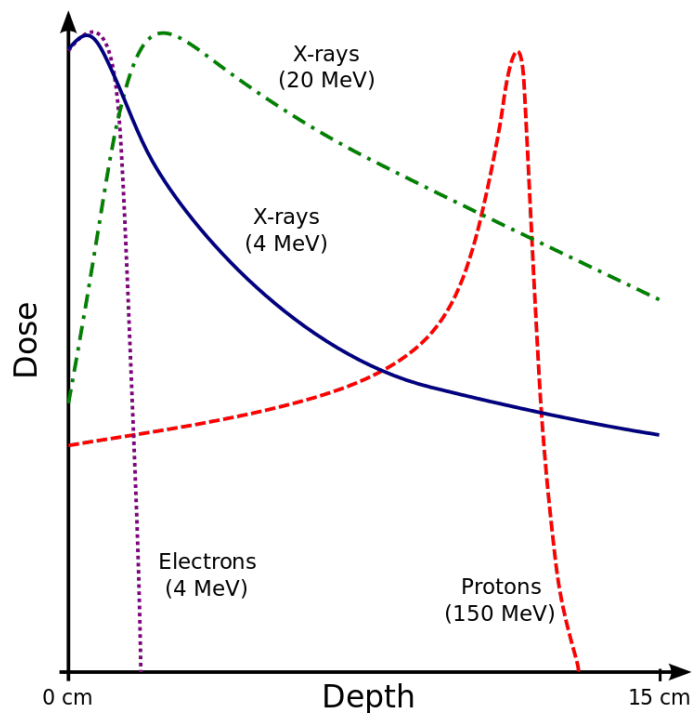


Figure 1.4: energy release of ionising radiation; [Cepheiden]

1.4.1 Role of CT

Until recently, radiotherapy treatment planning (RTTP) relied heavily on Computer Tomography (CT). There are two main reasons for this:

Firstly, CT uses low energy x-rays to create a 3D image of the patient. The luminosity value (brightness) assigned to each voxel (like pixel, but three-dimensional) corresponds to the local radiodensity recorded in Hounsfield units (*HU*). Materials with a higher radiodensity (e.g. bones) absorb more x-ray photons than those with less (e.g. water, brain-matter). Calculating the electron density using data obtained with CT is an easy task and used widely for RTTP. [9, 51] In order not to induce new cancer cells in healthy tissue during EBRT, the radiation beams are carefully targeted using the measured radiodensity. This way the absorbed dose accumulates in the cancer regions, while the nearby healthy tissue receives less radiation.

Secondly, CT images generate 3D images with little distortion. Exact geometries are needed for correct RTTP. Distorted images might lead to wrong calculations of how much energy is needed for the radiation to accumulate exactly at the target region. If, for example, bone structure is depicted as thicker than it really is, RTTP would suggest a treatment which would deposit more energy behind the tumour than intended. The opposite holds for cases where tissue appears to be thinner, which would result in areas lying before the tumour being irradiated. This is why CT images are preferred as they show little to no distortion.

Image of RTTP

1.4.2 Role of MRI

Today RTTP often combines CT images with data acquired using Magnetic Resonance Imaging (MRI). MRI scans also record luminosity values, but they do not correspond to *HU* (which is directly related to radiodensity, measured by CT). The signal intensity depends on other factors (see 1.3.3) and even varies between MRI scanners. Due to the better visibility of tumours on MRI images, RTTP often uses combined data from both imaging modalities. However, there are some difficulties arising from combining CT and MRI for EBRT: In order to profit from separately acquired data, the resulting images must be aligned either manually or automatically. This is a hard task since non-rigid objects (organs) change their shape and location between measurements which may lead to inaccuracies. Therefore MRI-only radiation therapy protocols are being developed: MRI data is used to create a Pseudo-CT, which contains information about electron density. Comparisons to using CT and MRI have shown acceptable deviations for X-ray therapy. In charged particle therapy the resulting dose gain in healthy tissue and dose loss in cancer regions owed to inaccurately assigned electron density values is bigger. However, current development is promising. [45, 57, 36, 17, 7]

1.5 Aim of this work

The idea of only using MRI for treatment planning seems close to realisation, but there are some issues that need to be addressed first. Due to the possible image distortion, great care needs to be taken and the images must be verified before they are used for RT target definition. The available MRI scanner at the AKH is equipped with an on board correction algorithm which is supposed to reduce distortion. The goal of this work is to commence the development of a quality assurance tool to asses the spatial distortion of the MRI scans (after applying the internal correction). This is achieved by comparing MRI images to CT images used as a gold standard. An already existing custom designed phantom is provided by the AKH Vienna for this purpose. However, the liquid to fill the rods with has not been chosen yet. Therefore, this work focuses mainly on the acquired data and which liquids to use the phantom with, not its entire design. However, possible fillings have to be produced and tested. Similar approaches are being used for distortion correction by other facilities. [42, 39, 58, 62, 63, 33] (TODO: more spectacular!)

2 Material and methods

2.1 Scanners

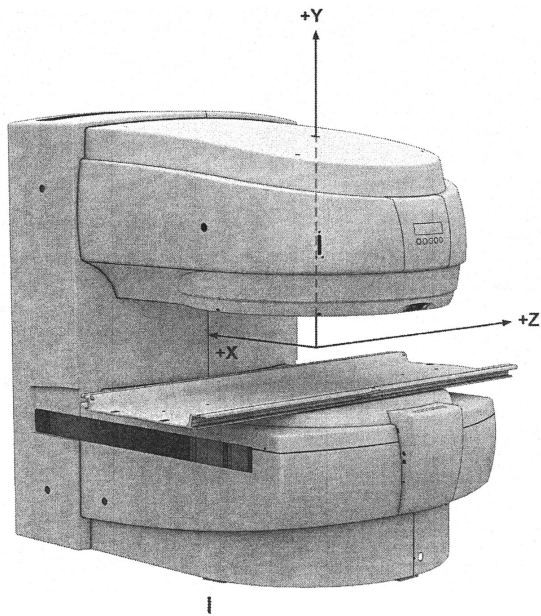
The radiation oncology department of the Vienna General Hospital (AKH) owns a open-bore, c-arm MRI scanner and a CT scanner (used as reference). They are listed in Table 2.1.

System	product name	company	coil [internal W x H]
MRI	Magnetom C!	Siemens	Body/Spine Array Coil XL [50 x 30.5 cm (19.7 x 12 in)]
CT			—

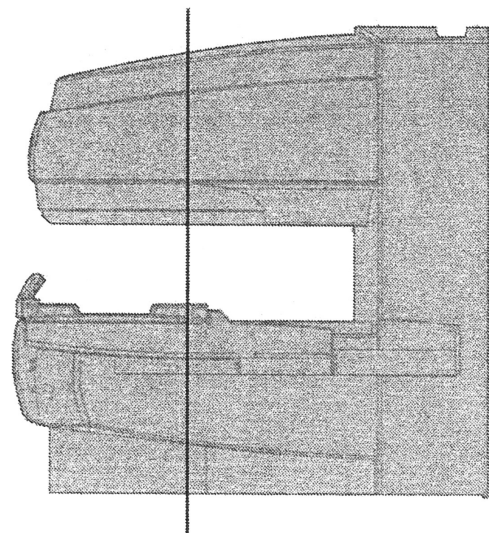
Table 2.1: used scanners

2.1.1 MRI scanner - field distribution

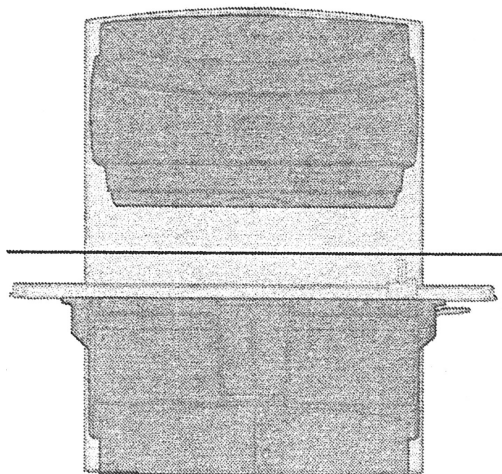
The Magnetom C! MRI scanner comes with a handbook which contains diagrams of the magnetic field strength (fig. 2.2), and its gradient (fig. 2.3, 2.5, and 2.4). Figure 2.1 shows an image and different views of the scanner and the planes along which the field strength and gradient are displayed.



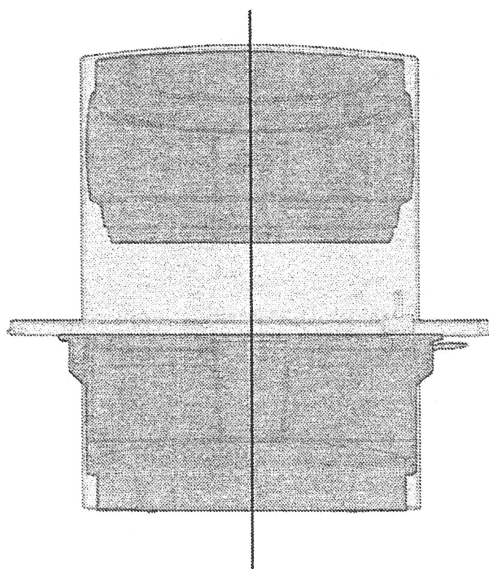
(a) Image of scanner
x,y, & z -axis



(b) side view along z-axis,
black line represents plane for
front view (see fig. 2.4)



(c) front view along x-axis,
black line represents plane for top
view (see fig. 2.5)



(d) front view along x-axis,
black line represents plane for side
view (see fig. 2.3 and 2.2)

Figure 2.1: Magnetom C! [magnetom_handbook]

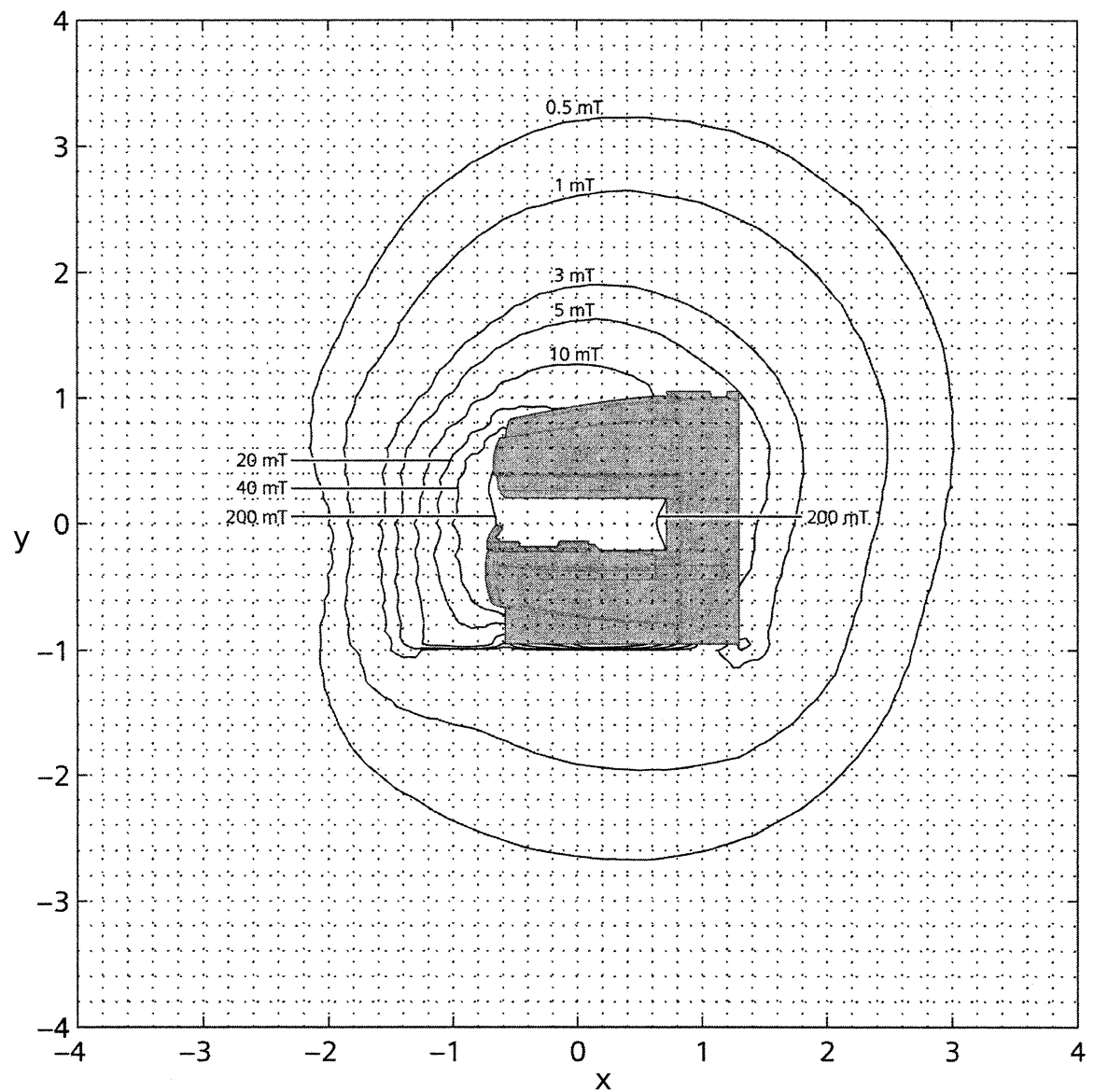


Figure 2.2: Magnetom C! field strength
side view along z-axis (see fig. 2.1d) [magnetom_handbook]

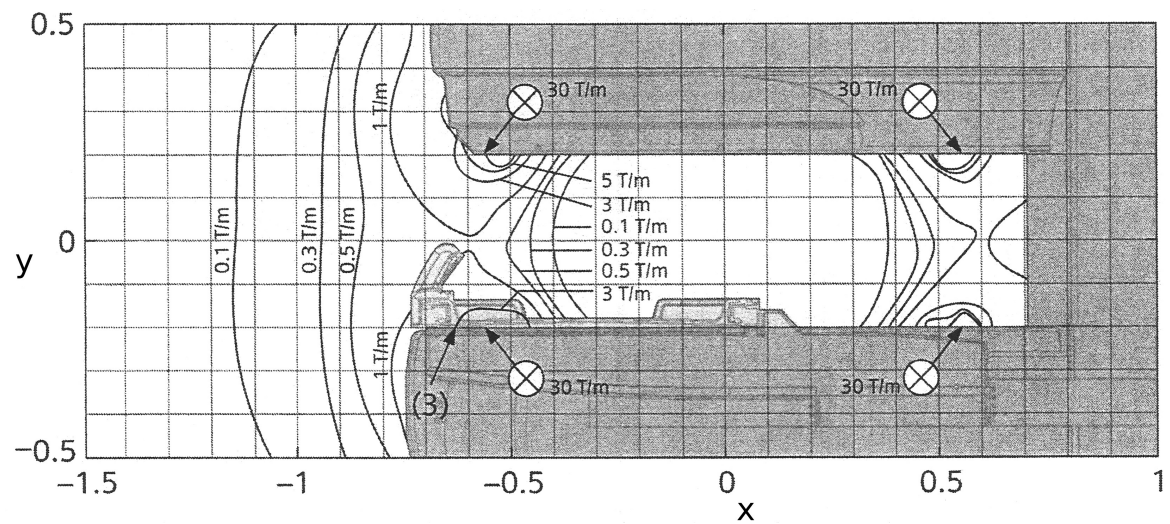


Figure 2.3: Magnetom C! field gradient
side view along z-axis (see fig. 2.1d) [magnetom_handbook]

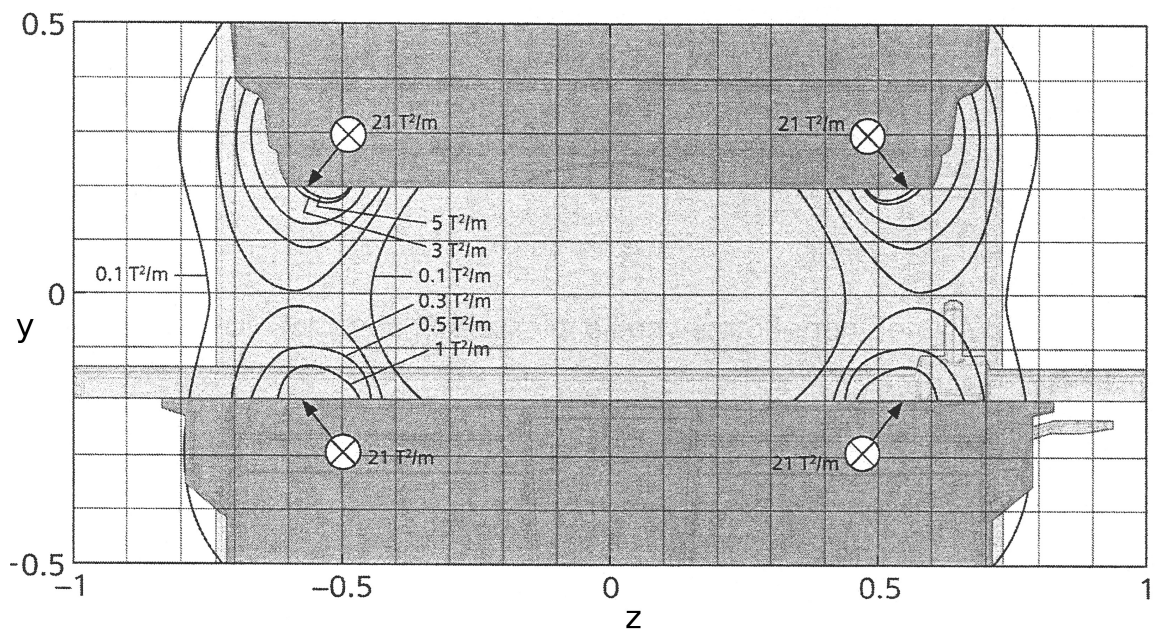


Figure 2.4: Magnetom C! field gradient
front view along x-axis (see fig. 2.1b) [magnetom_handbook]

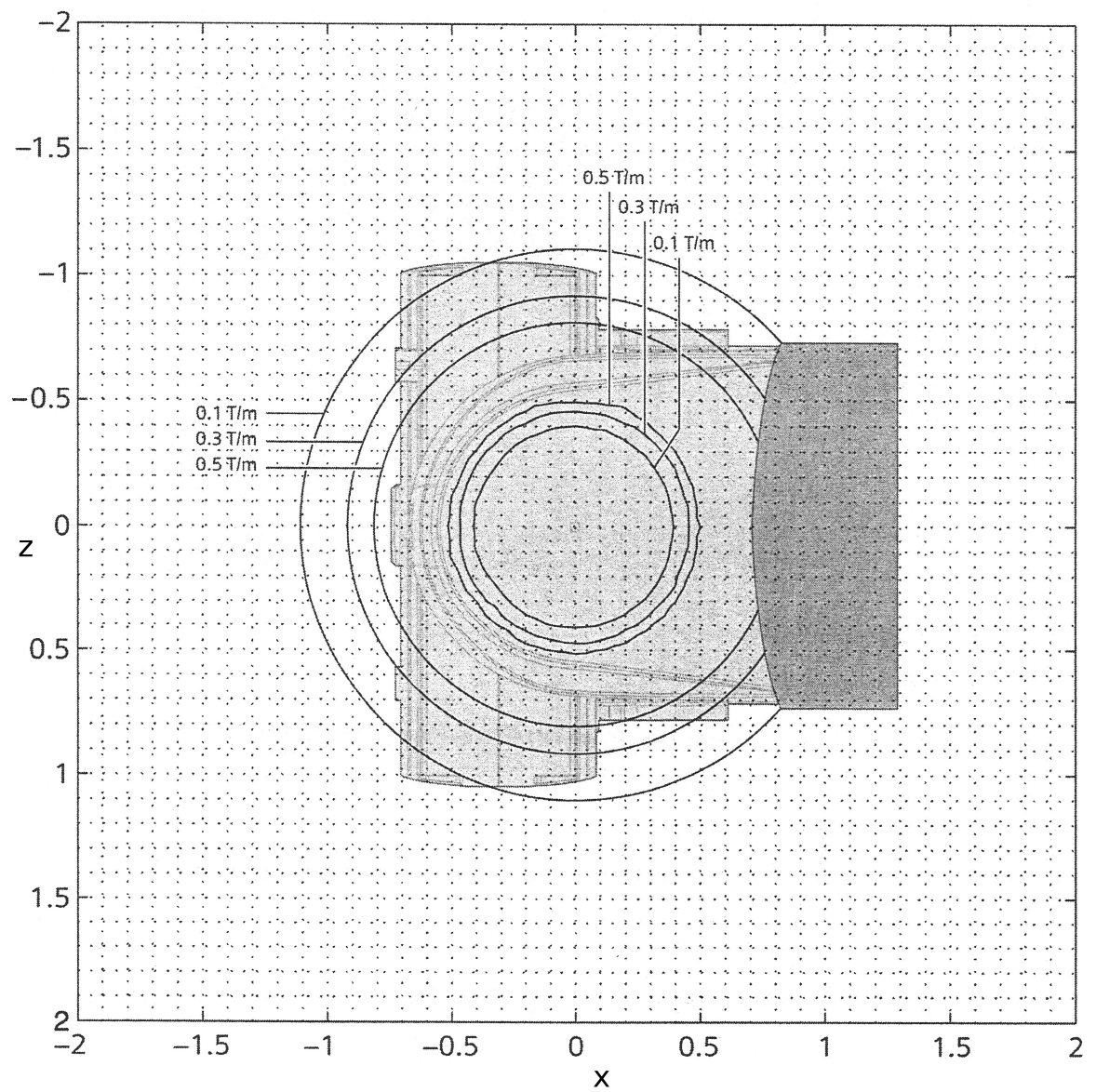


Figure 2.5: Magnetom C! field gradient
 top view along y-axis (see fig. 2.1c) [magnetom_handbook]

2.2 Custom build phantom

To compare images from different scanners and asses occurring distortion, a rigid object with known dimensions is necessary. Such a 'phantom' is often made from plastics containing a liquid. The AKH's design is made up from an array of replaceable, fillable plastic rods.



Figure 2.6: Comparison: MRI only shows liquid filling, CT also the plastic rod and pane (horizontal black bar crossing middle and right rod);
(a:) *MRI* - filled rod, plastic not visible (field of view too small to show entire rod); (b:) *CT* - empty rod, plastic visible; (c:) *CT* - filled rod, plastic and filling visible

2.2.1 Frame and rods

The phantom was build to fit the largest available rigid coil for the MRI scanner. Three parallel acrylic glass panes in the shape of the coil serve as a frame for the plastic rods. In the middle an empty area was reserved for an optional additional smaller phantom (not used for this work). Figure ?? shows a picture of the phantom. See also figure 2.7 showing a CT image of one pane (with no rods inserted).

More than 300 plastic rods (length: 50cm, outer diameter: 8mm, inner diameter: 4mm, volume: approx. 6mL) could be placed in the phantom. See figure 2.8 for a schematic sketch of one rod. The bottom part of each rod was sealed with a hot glued plastic plug,

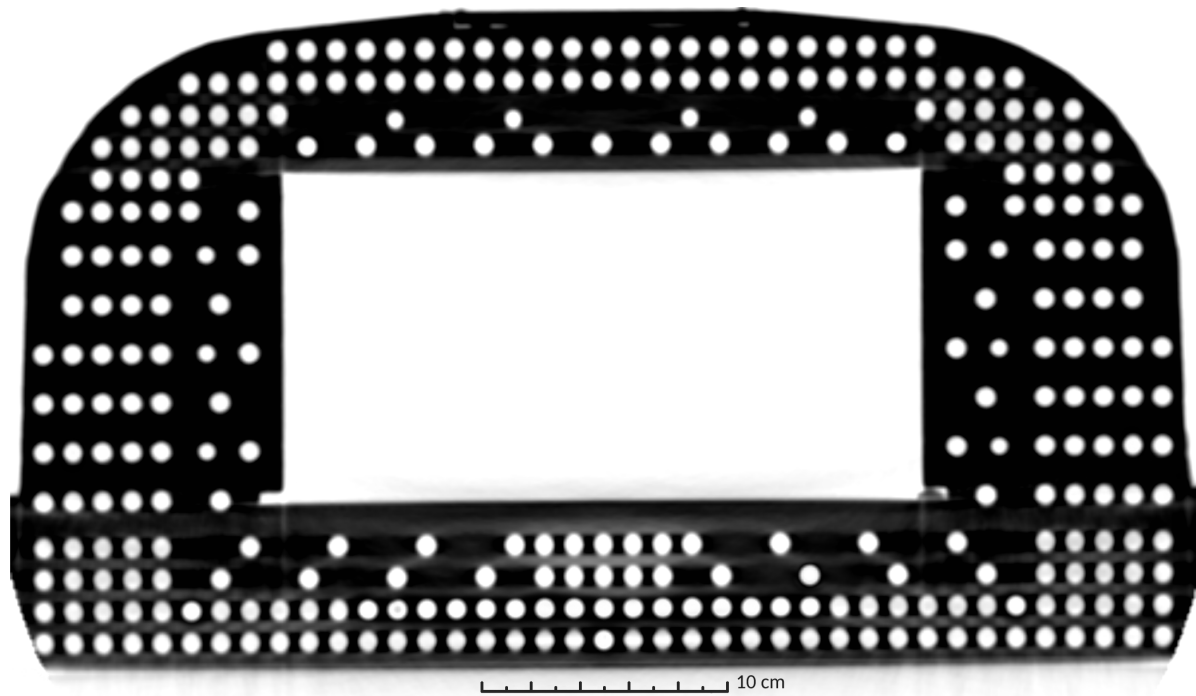


Figure 2.7: plastic pane, no rods inserted

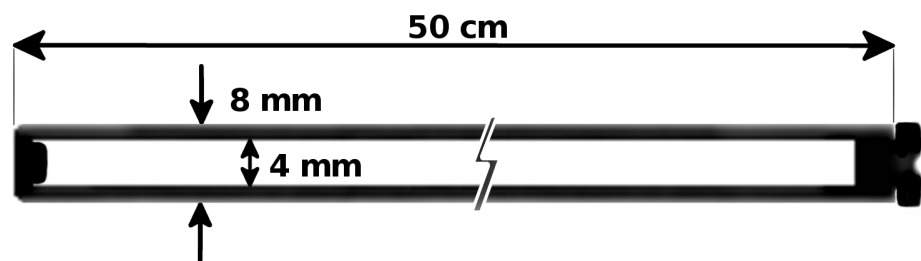


Figure 2.8: empty plastic rod, schematic (not true proportions);

the top could be closed with a plastic screw. Frame and rods were already build and assembled before the author started working on this project.

photo of Phantom photo of single rod

2.2.2 Rod fillings

For this study 17 different liquids were produced to be tested as possible fillings. They are listed in Table 2.2.

No.	$NaCl$	$CuSO_4 \cdot 5H_2O$	Soap	Ascorbic Acid	Agar	Primovist [volume-%]
#1						
#2	3.6		1.96			
#3	3.6		3.92			
#4	3.6		19.6			
#5	3.6		1.96	1		
#6	3.6		1.96	5		
#7	3.6		1.96	20		
#8	3.6		1.96		0.36	
#9	3.6		1.96		3.6	
#10	3.6		1.96		36	
#11	3.6					0.1%
#12	3.6					1%
#13	3.6					10%
#14	3.6		1.96		0.5	
#15	3.6		1.96		20	
#16		Motor Oil:	<i>Castrol Power1</i>			
#17		Silicon Oil:	<i>Charge: 15HLVY023</i>			

Table 2.2: composition of tested solutions
(components in g/L ; exception: Primovist in volume-%)

- #1 distilled water
- #2 $NaCl + CuSO_4 \cdot 5H_2O$
- #3 increased concentration of $CuSO_4 \cdot 5H_2O$
- #4 further increased concentration of $CuSO_4 \cdot 5H_2O$
- #5 generic washing-up *soap* added to #2
- #6 increased *soap* concentration
- #7 further increased *soap* concentration
- #8 *ascorbic acid* added to #2
- #9 increased *ascorbic acid* concentration
- #10 further increased *ascorbic acid* concentration
- #11 *Primovist*
- #12 increased amount of *Primovist*
- #13 further increased amount of *Primovist*
- #14 agar
- #15 increased agar concentration
- #16 synthetic motor oil
- #17 silicon oil

Being closed at one end and having a capillary shape (small diameter) makes it impossible for the rods to be filled by pouring in the liquid. Instead of adding the fluid at the top, it has to be injected starting at the bottom. This way the contained air would be pushed out by the injected liquid through the opening at the top. A thin plastic tube was inserted and used for injection, leaving enough room for the gas to escape. Between injections of different liquids, the tube was flushed with #1 (distilled water) or #2 (main component of most solutions).

In order to minimise the amount of gas dissolved, the liquids were brought to boil shortly before injecting. Gas solubility generally decreases with rising temperature [19, 50]. After injecting the solution in the rods, they were left to cool down. Before closing, the rods were topped up completely (no trapped air bubbles). The oil based liquids, #16 and #17, were not brought to boil. Number #14 could be injected without problems, the solution remained fluid even after reaching room temperature. Number #15 on the other hand changed to a gel like consistence and clogged the tube right after the rod was filled. The tube could not be used again.

2.3 Sequences

(TODO: elaborate!) Following the suggestions given in the Report of AAPM MR Subcommittee TG1 “MR Acceptance Testing and Quality Control” [21], T1 weighted sequences were chosen to evaluate the possible solutions. (Table 2.3)

System	—	—	—	—
MRI	-	-	-	-
CT	-	-	-	-

Table 2.3: used sequences

2.4 Developed software tool

In order to asses the distortion of the MRI scanner, a tool was programmed. It is written in Python 2.7 and uses the *SimpleITK* package to read and process *DICOM* (“*Digital Imaging and Communications in Medicine*”) files. [44, 13] *SimpleITK* is a object-oriented “C++ library with wrappers for Python, Java, CSharp, R, Tcl and Ruby”. [52, 54] It’s versatility is one of the reasons why this approach was favoured. It is a simplified layer built on top of the National Library of Medicine Insight Segmentation and Registration Toolkit (ITK). *SimpleITK* is also used by Applications like *3D Slicer* , a “free and open source software package for visualisation and medical image computing”. [1, 23] For this work *3D Slicer* was used to crop images, quickly read values and visualise the results. Documentation and code examples of *SimpleITK* can be found at [53, 25] An alternative way to handle *DICOM* data in Python would be *Pydicom*. [43, 24]

An extensive list of packages used to process data:

- *SimpleITK*
- *numpy*
- *scipy*
- *matplotlib.pyplot* [20]
- *skimage.draw*
- *datetime*
- *os*

2.4.1 Processing MRI and CT scans

Prior to analysing their data, the scans had to be prepared. Figure 2.9 gives an impression how the steps performed affected the data.

- Step 1** To start with, they were aligned in a way that yields maximum overlap especially in the centre of the image using *MIRADA*.
- Step 2** However, the MRI image had a lower resolution than the CT scan. Therefore, the MRI voxel's size were changed to match the CT voxels. Both images were resampled to CT resolution and exported using *MIRADA*.
- Step 3** Both layers (MRI and CT) were loaded into *3D Slicer* (Version: Slicer-4.5.0-1-linux-amd64)
- Step 4** Its module 'annotations' was used to set a new region of interest (ROI) to include only a single rod.
- Step 5** With the module called 'crop volume' (setting: voxel based cropping) the scans were reduced to show only the selected ROI.
- Step 6** Using the module 'resample scalar volume' a number of interpolated (setting: 'bspline') higher resolution copies were created.
- Step 7** All data sets and the cropped original CT/MRI images were exported with 'create a dicom series' and saved in separate folders.

After this procedure a number of data sets based on the original CT and MRI was available, which all had the same number of slices along the z-axis parallel to the phantom's rods. Each pair (CT+MRI) has the same pixel spacing (/resolution) in x and y direction. See table 2.4 for more details. Figure 2.10 depicts 3 CT/MRI scans of a single rod (axial) with different resolutions. "x1" stands for the original CT scan resolution (MRI resampled to match). "x4" is a resolution resulting in 1 pixel being split in 4 smaller pixels, "x9" in 9, and so on and so forth. For better visibility, images shown as figures in this work are printed with inverted colours. Dark pixels have a high density/intensity value, white pixels are equivalent to air (low density/intensity).

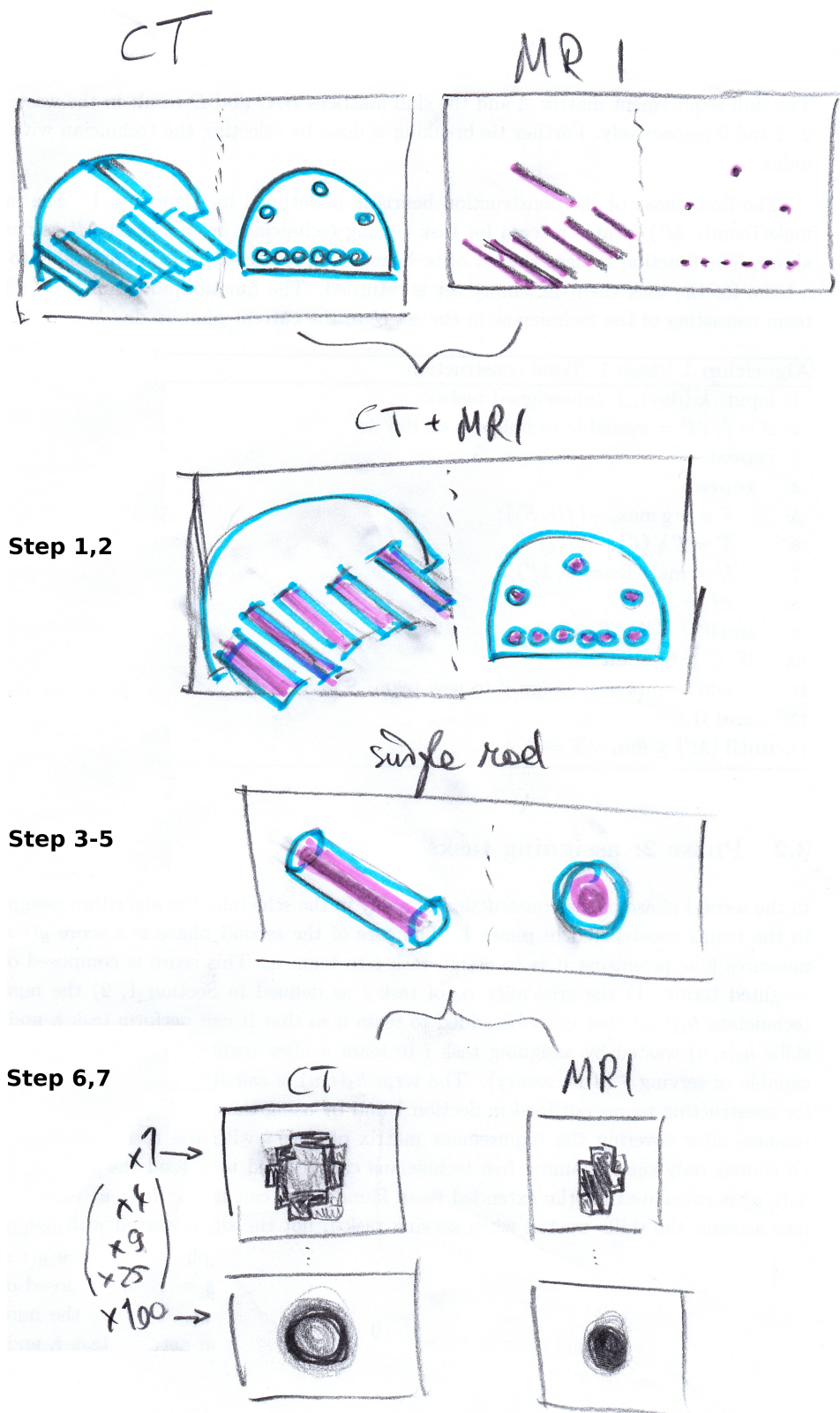
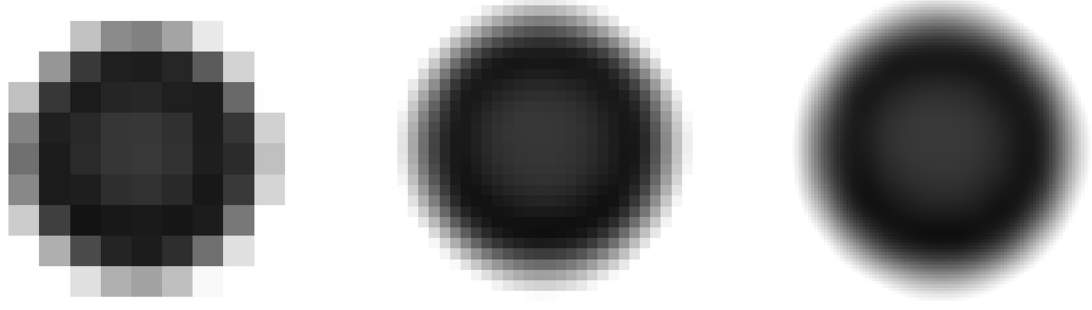


Figure 2.9: Steps performed before analysing data with script

resample factor	z (not affected)	y (same as x)	x
x1	0.60	0.98	0.98
x4	0.60	0.49	0.49
x9	0.60	0.33	0.33
x25	0.60	0.2	0.2
x100	0.60	0.2	0.1

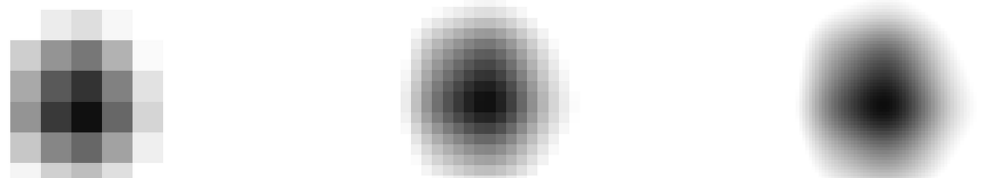
Table 2.4: pixel Spacing (rounded values) [mm]



(a) CT x1

(b) CT x9

(c) CT x100



(d) MRI x1

(e) MRI x9

(f) MRI x100

Figure 2.10: CT/MRI: axial image of single rod, filling #5 (inverted colours)

2.4.2 Capabilities

The developed software tool is not able to automatically detect individual rods shown in a CT or MRI scan. Instead the acquired 3D images have to be cropped to depict only a single rod.

The python script can:

- denoise the image data
- accepts coordinates to be used as seeds, enabling it to separate bright areas which are not connected ('masking' might be used as future method to automatically detect individual rods)
- calculate the centroid coordinates along the rod, used to
 - measure the local distortion
 - location shift
 - dice coefficient (roundness/deformation)
- plot individual rod slices
 - overlays one or two centroid coordinates
 - and save it as ".png" file
- change the pixel values to reflect the distortion occurring along a rod (visualisation)
- write the calculated numbers to a ".txt" file

2.4.3 Measuring distortion

Two phenomena were chosen to reflect the amount of distortion occurring in MRI scans:

- 1) location shift ("warp")
- 2) deformation (deviation from circular profile "DC")

Since the rods have a cylindrical shape, distortion can only be assessed in radial direction. To make calculations easier, the z-coordinate was put parallel to the rods, x and y radial. Ideally, each slice ($z = \text{const.}$) should depict the bright circular profile of the liquid (+ plastic rod in CT) surrounded by black (air). To calculate the location shift between rods shown in CT and MRI, the coordinates of the centre of mass (COM) were subtracted. The location difference in each slice is saved as an array. Additionally, the absolute value of the coordinate shift (warpMagnitude) could be calculated.

The dice-coefficient "DC" (also known as Sorenson-Index) was chosen as indicator for the deviation from a circular profile. Again this value was calculated for every slice using either the CT or MRI scans.

To get a idea of the occurring distortion one should look at both the absolute value of coordinate shift and the dice-coefficient (DC). The DC ranges from 0 to 1. A value of 1 indicates a perfect circular shape. A low DC on the other hand could be caused by many things such as: little overlap (e.g. a ring or crescent shape); a very dark image hindering delineation of rod from background; a small circle with a radius close to a only a few pixels.

2.4.4 Calculation: dice-coefficient (DC)

The dice coefficient or Sorensen index [32] is defined as:

$$DC = \frac{2|A \cap B|}{|A| + |B|} \quad (2.1)$$

The implementation into python is based on the open source python package “Medpy”. [30] A part of it’s module called “metric” was adapted. [31] All pixels above a certain threshold will be counted as input A. The reference B is a circle whose midpoint is placed at the centre of mass (COM).

The calculation of the DC is done by comparing an binary image to a circle. The position of the circle’s centre and its radius is highly influencing the outcome. Both the circle’s centre and its radius were varied during the distortion assessment.

2.4.5 Calculation: center of mass (COM)

The calculation of the COM is done with help of the “scipy” python package. It’s module “ndimage” contains the function “*center_of_mass()*”, which returns the COM’s coordinates of a given input array. The values assigned to voxels in CT images lie in the range from -1024 HU (air) to around 200 HU (plastic rod). Before a meaningful result can be obtained, the values need to be shifted to be > 0 . Additionally, only pixels representing the rod or the liquid should be used for the calculation. Otherwise the almost black voxels surrounding the rod would influence the result. This error could be observed especially if the rod is not placed in the exact middle of the scan. As described earlier, the plastic rod is only visible in CT images. On the MRI scans solely the liquid contained in the rods is shown. Therefore, rods appear to be smaller on the MRI data. To find the relevant pixels two algorithms were developed:

- 1 calculating the number of pixels based on rod size
- 2 finding a COM resulting in good DC

add 1: The inner (4mm) and outer (8mm) diameter of the rods are known. So is the *pixel spacing* which represents the equivalent size of a voxel in *mm*. Calculating the number of pixels which make up the more or less circular profile of the rod in each slice is calculated as follows:

$$pixelNumber = (radius^2 \cdot \pi) / (spacing^2) \quad (2.2)$$

For CT images $radius = 4mm$, in MRI scans $radius = 2mm$. $spacing$ is the pixel spacing in x and y direction. Next the pixels are sorted by brightness. The top $pixelNumber$ pixels are then used to calculate the COM.

add 2: This algorithm is an iteration method. First it looks at the whole range of possible *pixelNumbers*, from 0% to 100%. It starts off by assuming that 50% is a reasonable guess for the number of pixels that show the rod and calculates the corresponding DC value. To find out whether more or less pixels would result in a better DC, it chooses two new guesses: One halfway from the lower limit (0%) to its current guess (50%) which is:

$$\frac{0 + 50}{2} = 25\% \quad (2.3)$$

and one halfway from the upper limit (100%) to its current guess (50%) which is:

$$\frac{100 + 50}{2} = 75\% \quad (2.4)$$

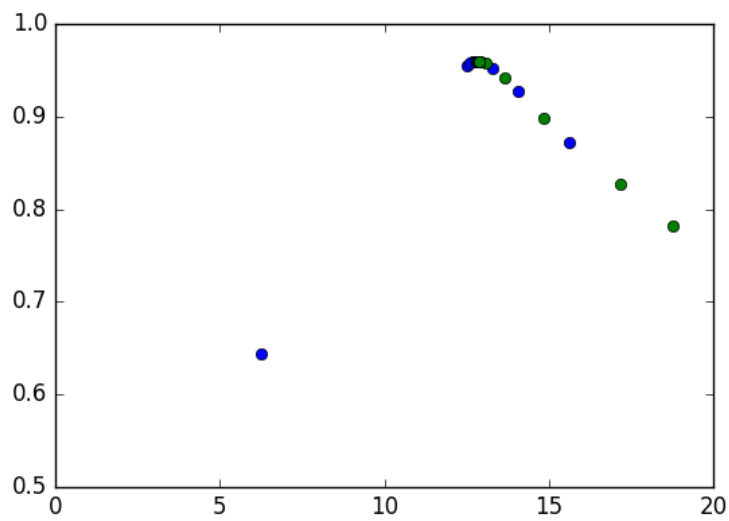
Now the corresponding DC values are calculated and compared. If the lower percentage yields a better DC, the upper half of the range will be neglected in the next iteration, the upper limit becomes the former guess (50%). If the higher percentage yields a better DC, the lower half of the range will be neglected in the next iteration, the lower limit becomes the former guess (50%).

Now in the second iteration, the range has become smaller and the next guess will be set to be exactly in the middle. If, for example, the DC for 25% was higher, the next

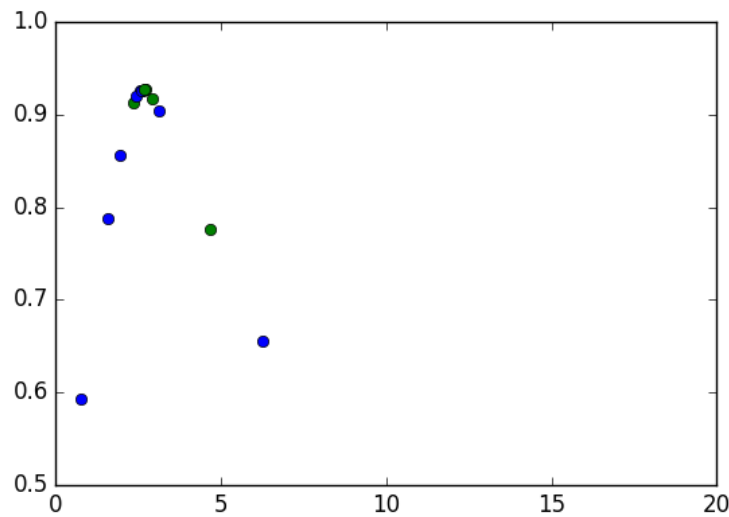
guess will be 25%, because the new range goes from 0% to 50%. In that case, DC values for the lower half of the range (12, 5%) and the upper half (18, 5%) will be calculated and compared. If, for example, the DC for 18, 5% was higher, the next guess will then be 18, 5%, because the new range goes from 25% to 50%. The iteration continues until new steps yield no better DCs or a set number of steps has been performed.

After the iteration process, the algorithm will return the COM which resulted in the best DC. Figure 2.11 shows the DC values found in the course of the iteration method. Figure ?? summarises the algorithm.

(TODO: flowchart for algorithms (send handwritten draft to Piotr))



(a) CT x100, (4 steps lead to best result)



(b) MR x100, (15 step performed)

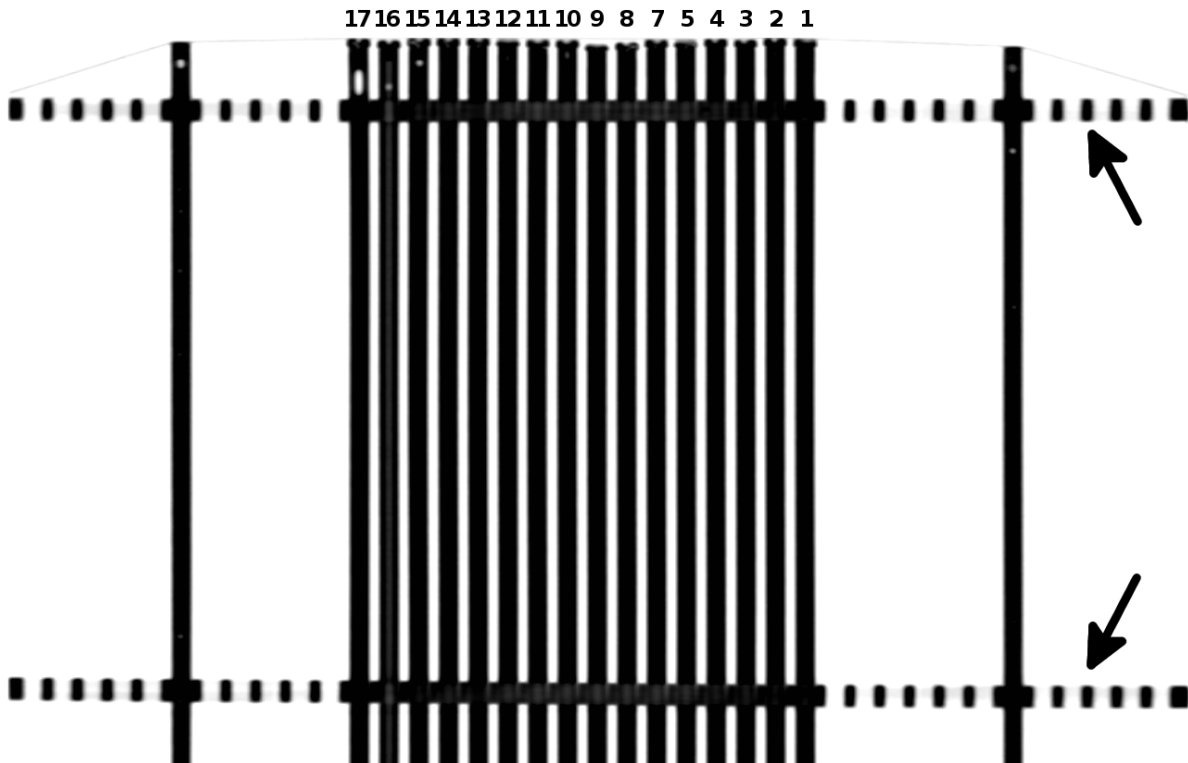
Figure 2.11: COM iteration method

3 Results

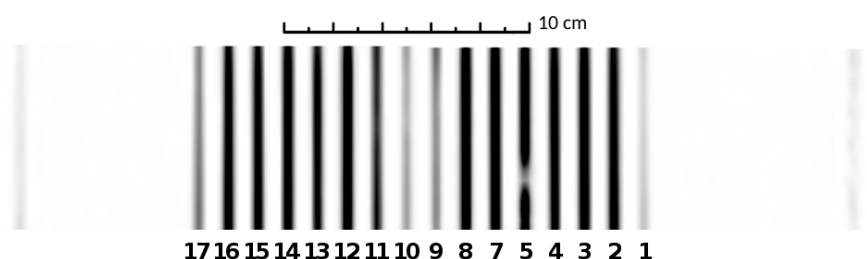
On the second day of working with the filled rods the one containing liquid #6 broke (leakage). It happened when delicately knocking it against on the table while standing upright. This was intended to mobilise bubbles that stuck to the wall and make them travel vertically to on end of the rod. (see tabular 3.2) The plastic stopper on the lower end came loose. The rod containing filling #6 was not replaced. Consequently, all CT and MRI images show only 16 rods.

3.1 Obtained MRI and CT scans

Figure 3.1 shows a coronal view of the 16 rods filled with the tested liquids. (in figure 3.2b a plastic bottle filled with water has been placed there instead (see figure 2.7).)

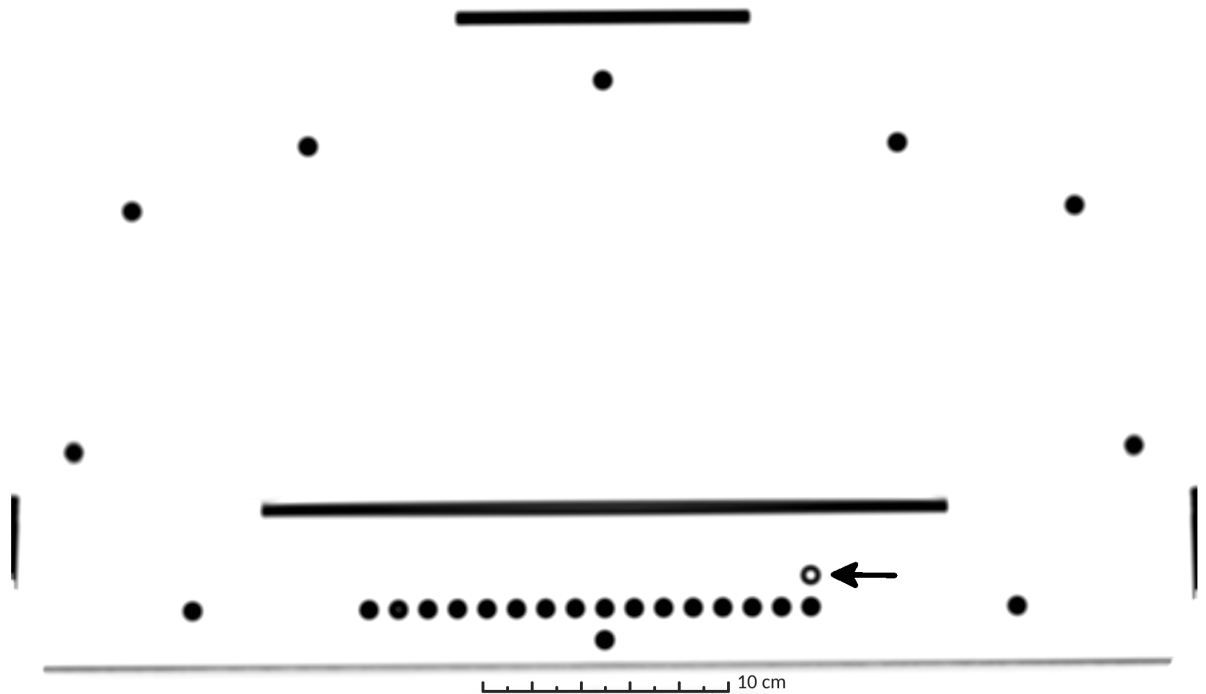


(a) CT: periodic black lines in upper and lower part of image (arrows) show plastic panes from above); rods have been fixed with adhesive tape (faint line across upper end of rods); differences in signal intensity (brightness) hardly noticeable, but air bubbles visible at upper end

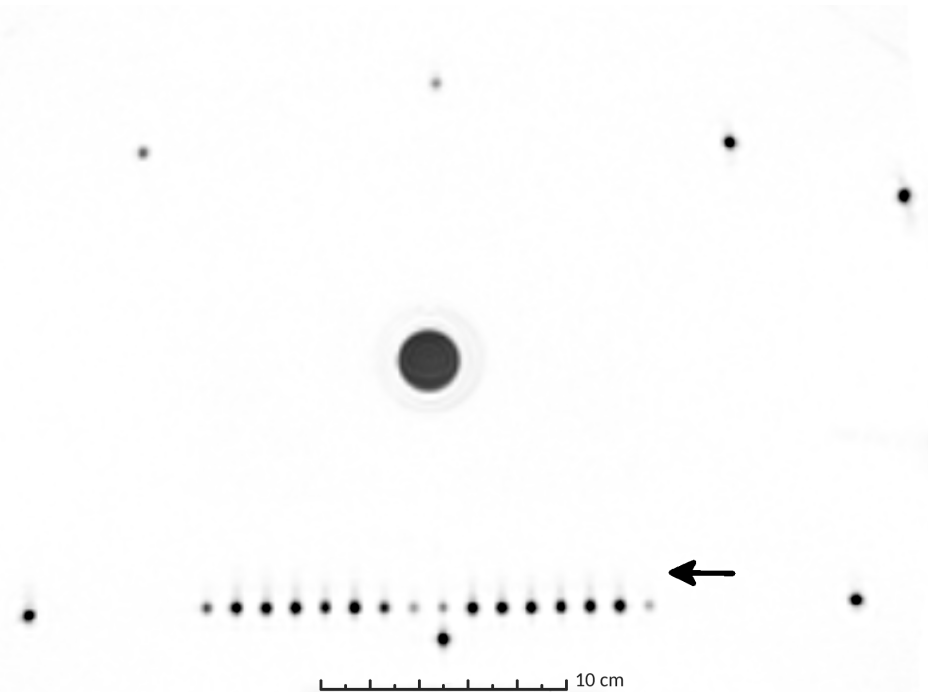


(b) MR: rods appear to be thinner, because only the liquid filling is visible; plastic (rods and panes) are not visible

Figure 3.1: Coronal CT/MRI (inverted colours; same scale; cropped images): images of 16 rods (tested liquids, numbering starting from the right, #6 excluded) + 2 reference rods (filled with water) on the sides; liquids result in different signal intensity (brightness)



(a) CT: black bars just above tested rods, at the very top and to the sides show plastic parts of the phantom holding it together; faint grey line below tested rods shows table on which phantom was positioned during imaging



(b) MRI: black circle in middle shows water bottle which was placed in the middle of the phantom (necessary for MRI scanner to start imaging)

Figure 3.2: axial CT/MRI (inverted colours, same scale): images of 16 rods (tested liquids, numbering starting from the right, #6 excluded); surrounded by reference rods (filled with water) and one empty rod (marked with arrow) which is not visible on MRI scans

3.2 Tested solutions

3.2.1 Visibility on CT/MRI scans

CT images show little differences between the tested liquids. The plastic rods themselves result in brighter pixels than any of the tested solutions.

On MRI scans most liquids had a mean and a max brightness value above 1000 (see table 3.1).

Only #1, #9, #10, & #17 resulted in significantly less signal (below < 1000).

No.	Min	Max	Mean	Median	RMS	σ
1	182	371	288	269	296,3	69,8
2	1044	1921	1443,8	1405	1477,3	312,9
3	941	2075	1451,2	1394,5	1508,9	413,2
4	1176	1709	1440	1437,5	1458,6	232,5
5	1125	2111	1583,8	1549,5	1623	355
7	971	2241	1466,8	1316	1540,6	471,2
8	1459	1947	1704	1705	1713,5	180,5
9	385	584	486,8	489	495,6	93
10	247	502	343,6	266	361,1	111
11	830	1268	1036,2	1023,5	1049	163,2
12	1158	2211	1648,8	1613	1695,2	394,2
13	836	1657	1146,8	1047	1190,9	321,2
14	800	2062	1383	1335	1461,7	473,1
15	1156	1829	1476,2	1460	1501,2	272,7
16	1102	1967	1509	1483,5	1543,8	325,8
17	356	938	629,6	602	668,1	223,6

Table 3.1: liquid visibility on MRI scan

3.2.2 Mechanical properties of solutions

The liquids were filled in a rod each and observed for several months. Each rod was free of bubbles directly after sealing. All rods containing water based solutions were filled with some air after 2 months and the amount of liquid continued to decrease further (see table 3.2). Knowing the inner diameter d of the rods we can easily approximate the volume of gas trapped:

$$V = \frac{d^2}{4} \cdot \pi \cdot l \quad (3.1)$$

In some of the tested rods the produced air bubbles would stick to the wall. Only after gently hitting the rod they would start moving.

While adding generic washing soap (#5, #6, and #7) did not hinder air bubbles from forming, it significantly improved their mobility. Not only did they move quickly when the rod was tilted, large quantities also did not block the entire diameter of the rod. Instead they formed large but cohesive bubbles that could be moved to one end of the rod easily and at no point sticked to the plastic wall.

The ascorbic acid present #8 (concentration of 0.36 g/L corresponds to approx. 0.00204 mol/L), #9 (3.6g/L), and #10 (\$36 g/L\$) seemed to have held back the formation of air bubbles for up to one week. After two months of observation, however, the rods also contained some air. It should be noted that the surface of the screw sealing the rod filled with #10 turned brown.

The rods filled with Primovist (#11 to #13) were filled with some air bubbles after at least two days. Moreover, the bubbles sticked to the walls of the rod and only shaking it violently made them move to one side of the rod.

It took more than a week until the rod containing the low concentration of agar (#14) contained an air bubble. The very slow running consistency made it impossible to coerce it to either end of the rod. Rod #15 on the other hand did not form bubbles in the middle of the rod, but seemed to have dried starting at the end with the plastic stopper.

No.	after 1 day		after 2 days		after 1 week	
	bubbles	hit req.	bubbles	hit req.	bubbles	hit req.
#1	yes	no	no		no	
#2	yes	yes	no		no	
#3	yes	yes	no		no	
#4	yes	yes	no		no	
#5	yes	no	yes	no	no	
#6	yes	no	<i>rod was leaking</i>			
#7	yes	no	yes	no	yes	no
#8	no		no		no	
#9	no		no		no	
#10	no ¹		yes	yes	yes	yes
#11	no		yes,	<i>sticked to wall</i>	yes	yes
#12	yes	yes	yes,	<i>sticked to wall</i>	yes	yes
#13	yes	yes	yes,	<i>sticked to wall</i>	yes	yes
#14	no		yes	no	yes	yes
#15	no		no		no	
#16	no		no		no	
#17	no		no		no	

No.	after 2 months	
	length of trapped bubble l [mm]	approx. volume V [mm ³]
#1	2	25.13
#2	1.8	22.62
#3	1+1 (air blockage, at lower end)	25.13
#4	4	50.27
#5	1.5 (many small bubbles)	18.85
#6	<i>rod was leaking</i>	
#7	2 (many small bubbles)	25.13
#8	2.3	28.90
#9	3	37.70
#10	2.4	30.16
#11	2	25.13
#12	2	25.13
#13	2.3	28.90
#14	1.5+0.5 (big immobile bubble, at center)	25.13
#15	3.4 (agar gel dried)	42.73
#16	0	0.00
#17	0.5	6.28

Table 3.2: solutions, observations

3.3 Distortion assessment

All results were obtained by manually cropping the 3D image to depict only a single rod.

(TODO: add slice which shows particular problem (e.g. high distortion, air bubble or artefact resulting in extra-hihg distortion value)) (TODO: rename xy axis, x-axis = distance from middle instead of slice number) (TODO: discuss what is visible on the graphs in discussion section)

3.3.1 Distortion

slice	$warp_x$	$warp_y$	$warp$	DC_{CT}	DC_{CT}^*	DC_{MR}	DC_{MR}^*	$DC_{MR(CT-COM)}$	$DC_{MR(CT-COM)}^*$	$warpDC$	$warpDC^*$
0	-0.11119	-1.0929	1.0986	0.9942	0.9942	0.9411	0.8619	0.6403	0.6427	0.0647	0.1517
1	-0.1283	-1.0923	1.0999	0.9932	0.9932	0.9438	0.8669	0.6453	0.6474	0.0618	0.1464
2	-0.1356	-1.091	1.0994	0.9922	0.9922	0.949	0.8744	0.6502	0.652	0.0561	0.1381
3	-0.1537	-1.0799	1.0908	0.9942	0.9942	0.9466	0.8821	0.6564	0.6585	0.0582	0.1286
:											
169	0.01	-0.6987	0.6988	0.9899	0.9899	0.9089	0.9515	0.7731	0.7784	0.0637	0.0339
170	0.0085	-0.6953	0.6954	0.9887	0.9887	0.9086	0.9512	0.7722	0.7775	0.0636	0.0339
171	0.0094	-0.6862	0.6863	0.9883	0.9883	0.9089	0.9509	0.7717	0.7771	0.0625	0.0337
172	0.0158	-0.6797	0.6799	0.9847	0.9847	0.9088	0.9509	0.7709	0.7763	0.062	0.0334
173	-1	-1	-1	-1	-1	0.9085	0.9505	-1	-1	-1	-1
174	-1	-1	-1	-1	-1	0.9089	0.9509	-1	-1	-1	-1
:	:	:	:	:	:	:	:	:	:	:	:
192	-1	-1	-1	-1	-1	0.914	0.9515	-1	-1	-1	-1
193	-1	-1	-1	-1	-1	0.9144	0.9518	-1	-1	-1	-1
194	0.0434	-0.7079	0.7092	0.9834	0.9834	0.9144	0.9524	0.7768	0.7819	0.0607	0.0337
195	0.0418	-0.7038	0.7051	0.9852	0.9852	0.9144	0.9524	0.7768	0.7819	0.0603	0.0335
196	0.0395	-0.7023	0.7034	0.988	0.988	0.9136	0.9529	0.7791	0.7841	0.0608	0.0331
197	0.0409	-0.6952	0.6964	0.9878	0.9878	0.9146	0.9532	0.7808	0.7856	0.0595	0.0326
:											
303	0.3294	-1.3923	1.4307	0.9864	0.9864	0.3453	0.3019	0.2962	0.2872	0.9367	0.9987
304	0.3949	-1.8074	1.8501	0.9877	0.9877	0.0957	0.0821	0.0725	0.0763	1.673	1.6981
305	-1	-1	-1	0.9897	0.9897	-1	-1	0	0	-1	-1
306	-1	-1	-1	0.9891	0.9891	-1	-1	0	0	-1	-1
307	0.4056	-1.9934	2.0343	0.991	0.991	0.0519	0.0444	0.0223	0.0303	1.9286	1.9439
308	0.3664	-1.9952	2.0285	0.9873	0.9873	0.1533	0.1321	0.0534	0.0667	1.7175	1.7605
:											
393	0.0967	-0.2562	0.2738	0.9862	0.9862	0.9357	0.9311	0.9098	0.9011	0.0176	0.0189
394	0.1032	-0.2628	0.2824	0.994	0.994	0.9349	0.9318	0.9068	0.9025	0.0184	0.0193
395	0.11	-0.2453	0.2688	0.9944	0.9944	0.9356	0.9338	0.9082	0.9045	0.0173	0.0178

Table 3.3: script generated data

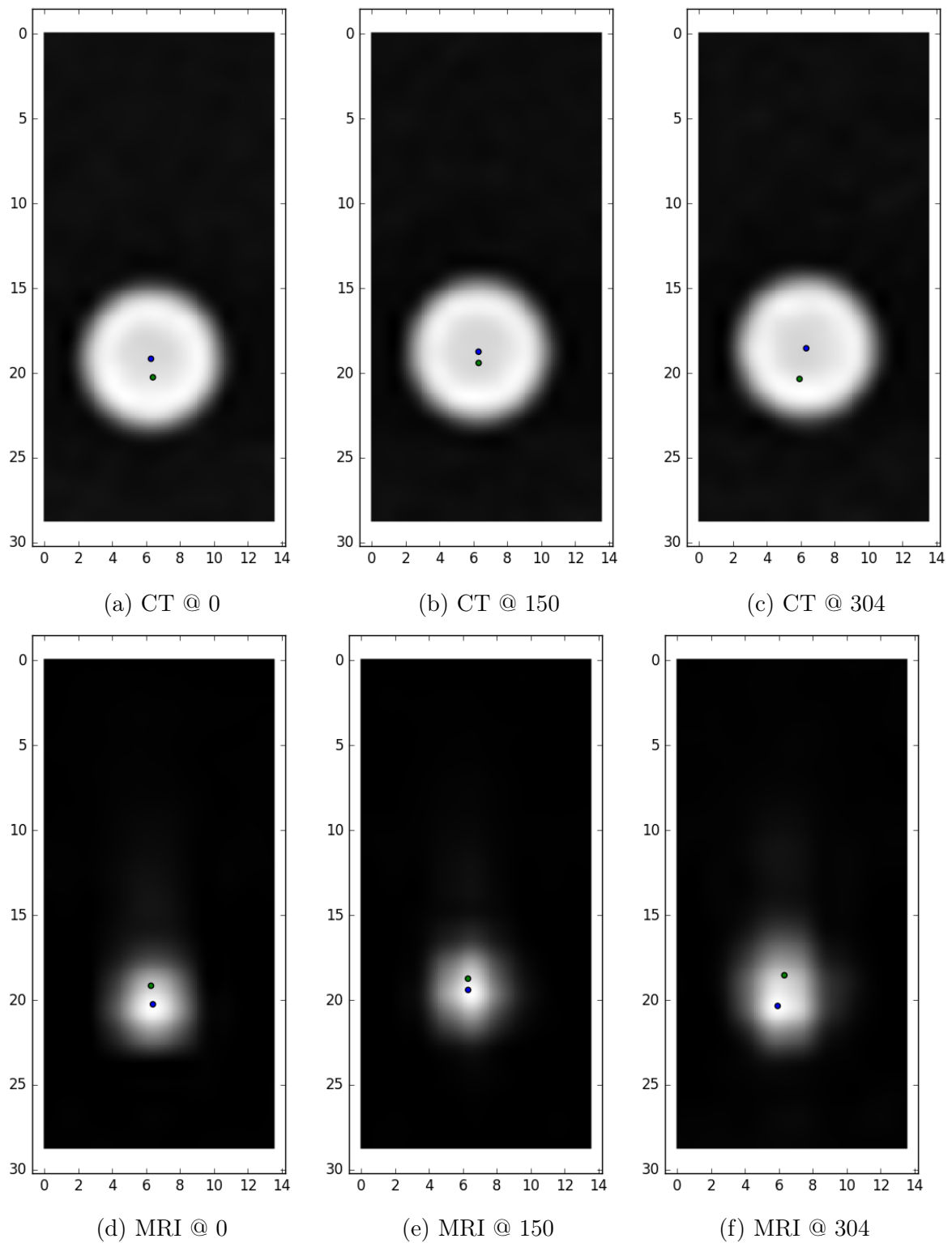


Figure 3.3: MRI x100; blue dot centroid MRI, green dot centroid CT (same scale); slice 150 is approximately at the isocentre, 0 on the very end of the image, 304 close to an air bubble

3.3.2 DC

The obtained dice coefficient varies not only because of the circle's centre and the radius, it also depends on the images resolution. Figure 3.8 and 3.9 show the DC (optimised) obtained using CT and MRI scans over resample rate.

(TODO: include table with actual RESULTS that are spit out by script and reference to python code (which will be in appendix)) (TODO: PIOTR: create colour coded images)

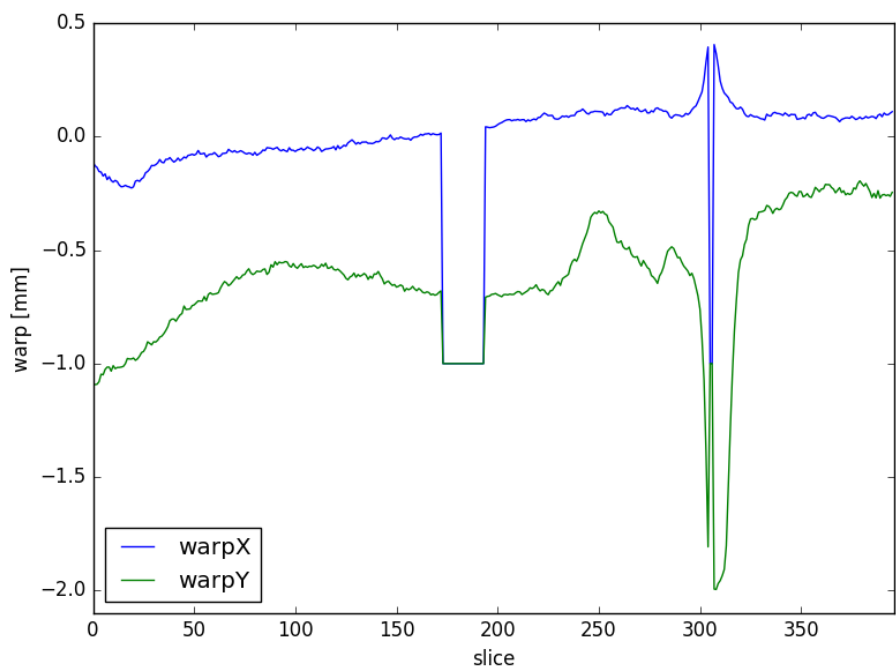


Figure 3.4: warp XY [mm], CT-MRI x100

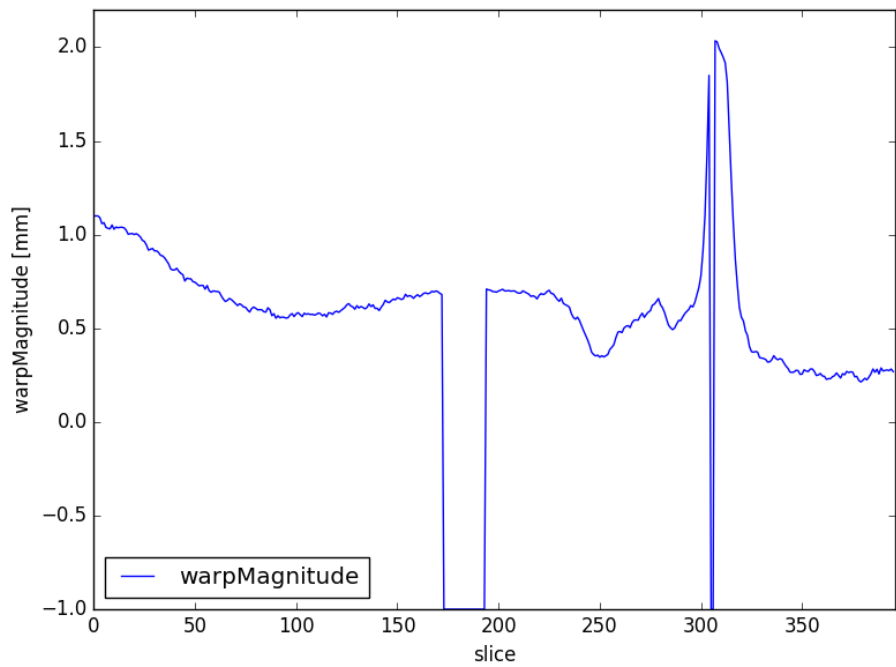


Figure 3.5: warp Magnitude [mm], CT-MRI x100

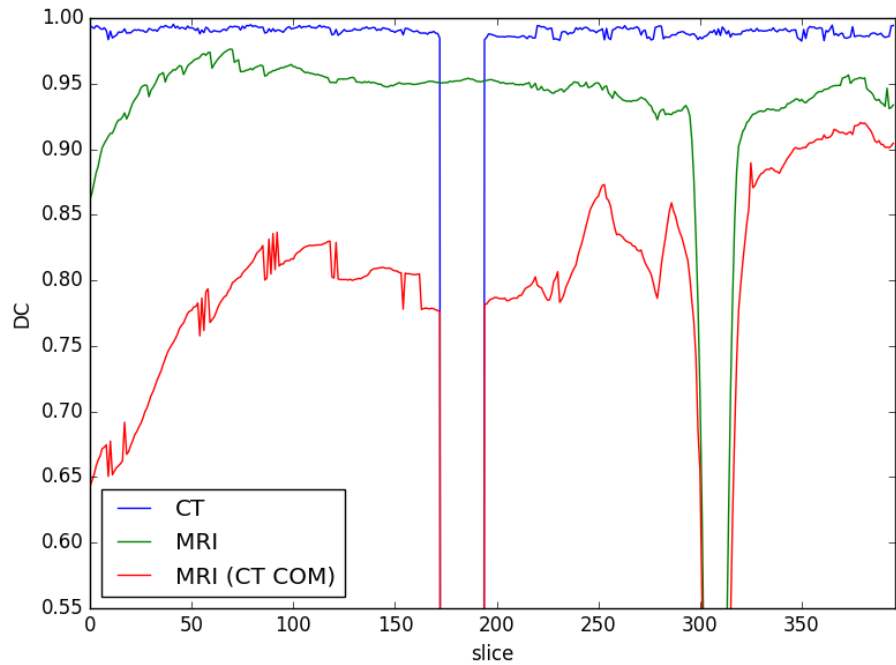


Figure 3.6: DC (optimised) for CT & MRI & MRI (using CT COM)

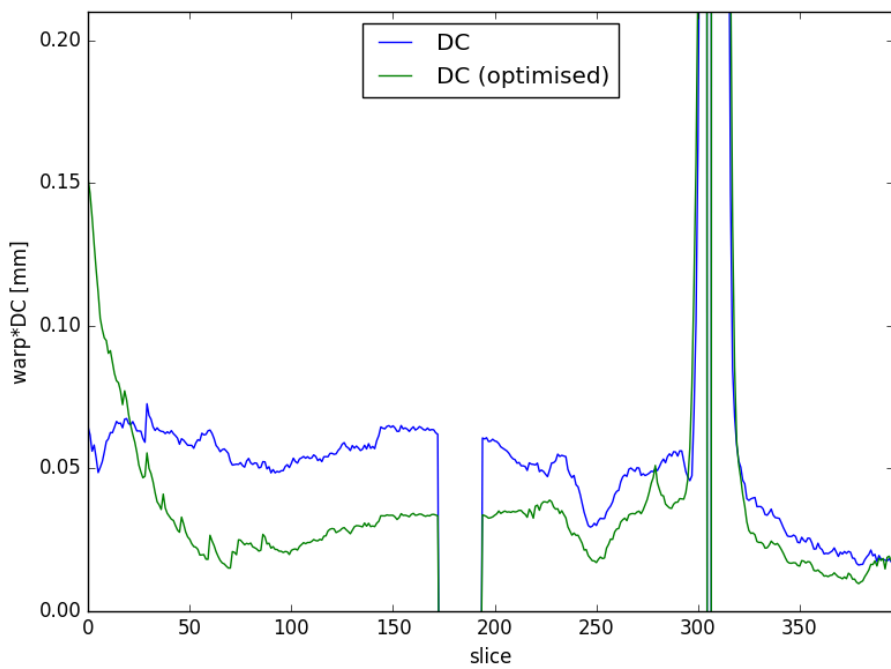


Figure 3.7: artificial indicator $warp^*DC$ using real DC and optimised DC of MRI x100

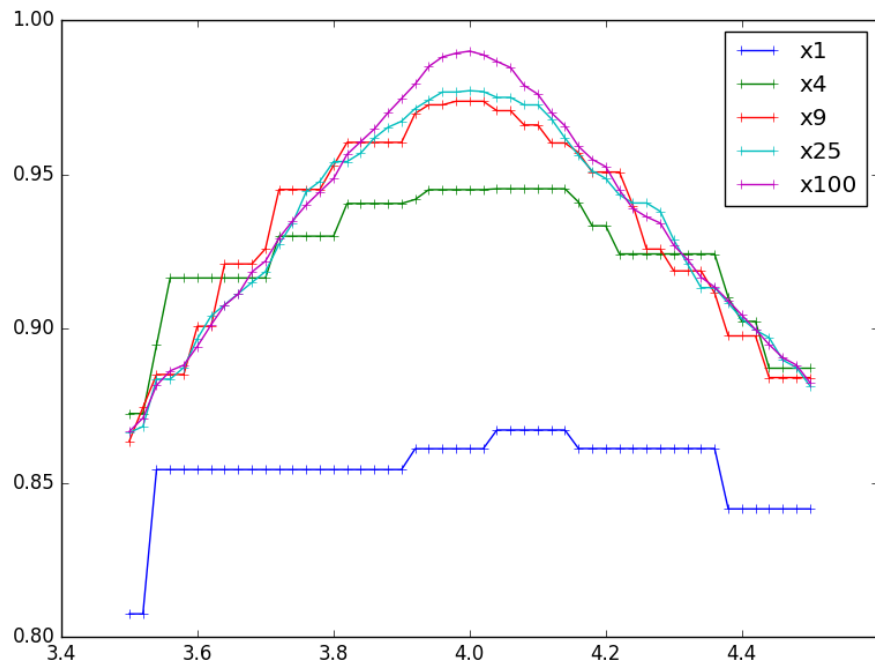
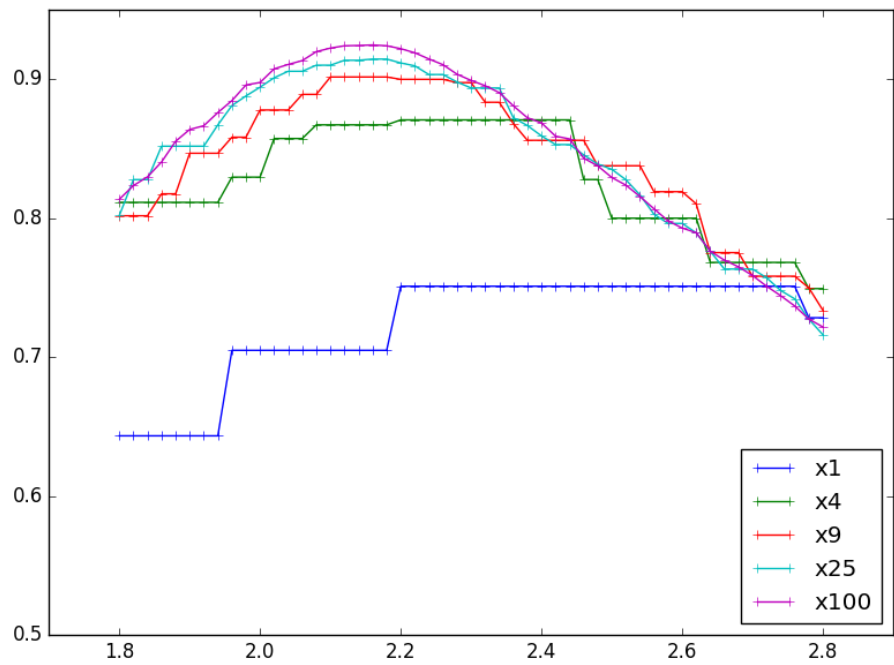
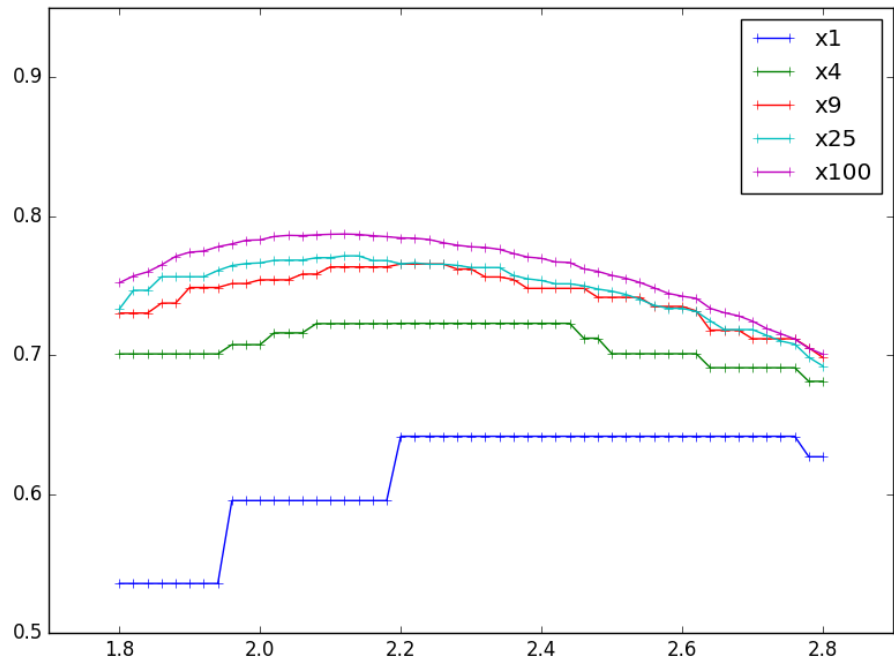


Figure 3.8: CT: DC of varied radii & resolutions



(a) MRI: DC of varied radii & resolutions



(b) MRI: DC of varied radii & resolutions (using CT-COM)

Figure 3.9

4 Discussion

4.1 Phantom design

To measure distortion the scanners must image a rigid object with known dimensions. Such phantoms are commercially available, but often expensive and designed for a specific calibration protocol. Some institutions build their own to fulfil exactly the requirements of a given application. The scanner used at the AKH is a relatively rare model, which is why there are only few available off-the-shelf phantoms that would fit its coil.

For the AKH it was important to create a lightweight phantom which can be imaged by CT and MRI scanners. Due to the underlying physics, plastics are not visible in MRI scans. CT however, also shows plastic. See figure 2.6 for a comparison (MRI/CT visibility). Therefore, they decided on plastic rods with a suitable fluid filling. Such a liquid should be easily produced, non-toxic, and yielding sufficient signal in MRI scans.

Commercially available phantoms often resemble water filled tanks containing plastic grids as a reference. This design results in stronger signal, but exceeds practical weight. There are few brands offering solutions utilising liquid fiducial markers in the shape of pellets. They are arranged in a regular pattern surrounded by air or plastic. The AKH's design however relies on replaceable rods, which makes it a novelty.

4.1.1 observed issues

Interestingly, all water based solutions seemed to have evaporated partly. This indicates that the plastic stopper is not closing the rod in a way that makes them airtight. An airtight container might have lead to other conclusions regarding the formation of air bubbles. It is hard to tell if they were caused by evaporation only or if dissolved gases played a role, too.

4.2 Tested solutions

For measuring the position of the rods in the CT scans, the plastic rods without filling would be enough already. Hollow plastic rods would not be visible on the MRI scans, though. That is why the visibility of the liquids on CT is not important at all. From now on 'signal (strength)' or 'visibility' will refer to MRI scans only (see table 3.1).

4.2.1 Thoughts about choosing possible candidates

The selection of solutions tested were chosen for a number of reasons:

1. Generally, imaging techniques aims for a high signal-to-noise ratio. Therefore, Liquids resulting in brighter pixels are favoured.
2. The amount of gas in the rods should be minimised.
3. If air bubbles form, tilting the entire phantom slightly should be enough to move them to one side. The FOW of the MRI scanner is too small to show the entire phantom anyway.
4. Most tested fluids are based on water, because this makes them easy to empty and clean. They could then be filled again with a different liquid if needed.
5. Preferably, the components which are chosen to be used for the entire phantom should be either non-toxic or harmless if not swallowed.

Rod #1 was filled with plain distilled water as reference. It was clear from the beginning that it would not result in high signal and was never considered a possible filling.

Aiming for high SNR

To achieve a better SNR, liquids #2 to #10 and #14 to #15 are based on a solution of sodium chloride ($NaCl$ concentration of 0.36 g/L) and copper(II) sulfate pentahydrate ($CuSO_4 \cdot 5H_2O$ concentration of 1.96 g/L as suggested by AAPM MR Subcommittee [21]; #3 and #4 contain double and ten-fold the concentration) in distilled water. Most of these liquids resulted in an about 5 times brighter signal than plain distilled water. Regarding the toxicity of $CuSO_4 \cdot 5H_2O$, the minimum dose to have caused acute toxic effects in humans is reported to be $11mg/Kg$. As the concentration of $CuSO_4 \cdot 5H_2O$ is only 1.96 g/L , even a young patient of 4 years and $15kg$ would need to drink more than

80mL to reach that threshold. Also, ingestion usually leads to vomiting triggered by its irritating effect on the gastrointestinal tract, which would stop further (more severe) toxic effects from happening. Keeping the scanner bed clean and checking the phantom for leakage before and after use should be sufficient to prevent an intoxication.

Primovist (#11 to #13) is a common contrast agent used for MRI scans [59, 48, 40] intended to yield a strong signal.

Handling dissolved gas

Unfortunately, dissolved gases may eventually leave the liquid and form air bubbles.

To improve the mobility of trapped air bubbles, generic washing-up soap was added (#5, #6, and #7; suggestion by Data Spectrum Corporation [11]). The higher concentrations of soap were tested as reference. If the liquid should happen to leak from the rod, the relatively low concentration of soap would not add to its toxicity. For those reasons, and because the liquid is cheap and easy to produce, it appears to be a promising candidate.

Liquids #8 (0.36g/L), #9 (3.6g/L), and #10 (36g/L) contain ascorbic acid. Adding this is supposed to reduce forming of air bubbles by binding dissolved oxygen and eventually degrade to dehydro-ascorbic acid and water. The amount suggested by [2, 4] is 0.00204 mol/L which corresponds to approx. (0.36g/L).

In an attempt to limit the forming of gas, *agar* was used in solutions #14 and #15. Agar and agarose are commonly used as basic reference material for MRI phantoms [6, 28]

Non water-based liquids

As an alternative 2 oils were proposed. Since air is not soluble in oil, once a rod is completely with oil, no air bubbles should form. Yet, oil is not as easily removed from a rod as a water based liquid. At the same time, it might not be necessary to ever replace the oil. Once filled, the rods could be used until the surrounding plastic breaks or starts leaking. Using vegetable oil would be a non-toxic solution, but has been ruled out as

a filling from the beginning, because it would eventually rot. Mineral oil on the other hand does not rot, however, it might be dangerous if not handled properly as it might leave toxic traces on the MRI scanner bed.

4.2.2 Choosing a promising candidate

As all rods containing water-based liquids continued to lose liquids due to evaporation, only the early forming of air bubbles might indicate whether solutions effectively hinder dissolved gases to result in trapped air bubbles. Apart from the solutions containing ascorbic acid (#8 (0.36g/L), #9 (3.6g/L)) all water based liquids produced some air bubbles after at least two days (see table 3.2.2). Considering the low visibility of #9, the only suitable water based liquid capable of staying free from air bubbles might be #8. At the same time, long-term observations might have shown that even #8 only delays the formation.

The reason why the rod containing the highest concentration of ascorbic acid showed an unexpected colouring is not known. Whether this is due to a contamination or a unforeseen chemical reaction involving the high concentration of ascorbic acid is unclear. As the high concentration in #9 and #10 led to a radical reduction in signal with the tested MRI sequence, this solution is not considered a suitable filling anyway.

Primovist (#11 to #13) lead to a good signal, but its limited mobility of air bubbles rules it out as a candidate.

If the forming of a small amount of gas is not considered a problem, adding soap appears to be a reasonable solution. The smallest tested amount of soap (#5, 1 g/L) was already enough to result in sufficient mobility of air bubbles, and an even lower concentration might also be acceptable. Interestingly, the rod filled with this solution contained the least amount of gas after 2 months, but this might be because the particular rod closed better than the others. The visibility recorded was among the higher candidates, too. For those reasons, and because the liquid is cheap and easy to produce, it is a promising candidate.

Solutions containing *agar* (#14 and #15) are even harder to remove from rods if not impossible. As they might lead to air bubbles, too, which cannot be moved to either side of the rod, agar is not suited for this phantom.

Finally, the generic motor (#16) oil resulted in the highest signal intensity of all candidates. Besides the question of its toxicity, it seems to be a good alternative to water based liquids. The silicon oil (#17) on, the other side, had a low signal compared

to most candidates and is therefore not suited.

4.3 Sequence

(TODO: why T1 weighted sequence? why this particular sequence? Influence on signal of water/oil, components.)

4.4 Distortion

An air bubble might lead to a incorrect COM. Without looking at the dice-coefficient it's hard to tell why this distortion only appears to be present in a few slices. If both indicators show unexpected local irregularities, a conclusion might be easier to draw.

(TODO: discuss what is visible on the graphs) (TODO: interpret data table spit out by script)

5 Conclusion and Outlook

5.1 Liquid for phantom

As topping up over 300 rods regularly is too time consuming, and all water-based liquids continued to evaporate, they are not long-term solution for this phantom. For short time experiments with this phantom (not airtight rods) #5 is recommended, because the soap allows the air to be moved out of the FOW. If a new set of (airtight) rods was obtained, adding ascorbic acid to the solution (a combination of #5 and #8) might be an even better filling:

- distilled water
- 0.36 g/L of NaCl
- 1.96 g/L of $\text{CuSO}_4 \cdot 5\text{H}_2\text{O}$
- 1 g/L of soap
- 0.36 g/L of ascorbic acid

In that case, the forming of air bubbles might be either avoided entirely (due to the ascorbic acid) or delayed and then easily taken care of by tilting the whole phantom slightly to move the bubbles out of the FOW. The long-term behaviour of the mix might lead to adverse properties and should be tested, though.

In the current set-up (not airtight rods), it seems best to fill the rods of the phantom type of oil that does not rot, but yields high signal. The tested generic motor oil (#16) fits those requirements. However, a non toxic alternative would be preferred.

5.2 Future improvement of software tool

The developed tool took a simplified approach to the problem by looking only at a single rod. Future improvements should enable the software to take into account all the rods automatically. This could be done by a auto-trace function which detects individual rods and applies the already implemented algorithms to each of them separately.

Distortion assessment can be performed using the generated tool, however, it needs to be implemented on more general scale to be able to measure the distortion for all the rods automatically

Bibliography

- [1] *3D Slicer*. \url{https://www.slicer.org/}.
- [2] S. M. Abtahi, Majid Shahriari, M. H. Zahmatkesh, H. Khalafi, Sh Akhlaghpoor, and S. Bagheri. “A new approach to contrast enhancement in MAGICA gel dosimeter image with MRI technique”. In: *Iranian Journal of Radiation Research* 6.3 (2008), pp. 151–156. ISSN: 17284562.
- [3] Christopher Bangard, Jennifer Paszek, Frank Berg, Gesa Eyl, Josef Kessler, Klaus Lackner, and Axel Gossmann. “MR imaging of claustrophobic patients in an open 1.0 T scanner: Motion artifacts and patient acceptability compared with closed bore magnets”. In: *European Journal of Radiology* 64.1 (2007), pp. 152–157. ISSN: 0720048X. DOI: 10.1016/j.ejrad.2007.02.012.
- [4] Richard S. Bodannes and Phillip C. Chan. “Ascorbic acid as a scavenger of singlet oxygen”. In: *FEBS Letters* 105.2 (1979), pp. 195–196. ISSN: 00145793. DOI: 10.1016/0014-5793(79)80609-2. URL: <http://doi.wiley.com/10.1016/0014-5793{\%}2879{\%}2980609-2>.
- [5] D. J. Brenner, C. D. Elliston, E. J. Hall, and W. E. Berdon. “Estimated risks of radiation-induced fatal cancer from pediatric CT”. In: *American Journal of Roentgenology* 176.2 (2001), pp. 289–296. ISSN: 0361803X. DOI: 10.2214/ajr.176.2.1760289. arXiv: 01/1762âĂ§289 [0361-803X].
- [6] M L Bucciolini Ciraolo and B Lehmann. “SIMULATION OF BIOLOGIC TISSUES BY USING AGAR GELS AT MAGNETIC RESONANCE IMAGING”. In: *Acta Radiologica* 30.6 (1989).
- [7] Lili Chen, Robert A. Price, Lu Wang, Jinsheng Li, Lihong Qin, Shawn McNeeley, C. M Charlie Ma, Gary M. Freedman, and Alan Pollack. “MRI-based treatment planning for radiotherapy: Dosimetric verification for prostate IMRT”. In: *International Journal of Radiation Oncology Biology Physics* 60.2 (2004), pp. 636–647. ISSN: 03603016. DOI: 10.1016/j.ijrobp.2004.05.068.

- [8] Aaron M. Coffey, Milton L. Truong, and Eduard Y. Chekmenev. “Low-field MRI can be more sensitive than high-field MRI”. In: *Journal of Magnetic Resonance* 237 (2013), pp. 169–174. ISSN: 10960856. DOI: 10.1016/j.jmr.2013.10.013. arXiv: NIHMS150003.
- [9] C Constantinou, J C Harrington, and L a DeWerd. “An electron density calibration phantom for CT-based treatment planning computers.” In: *Medical physics* 19.2 (2012), pp. 325–327. ISSN: 00942405. DOI: 10.1118/1.596862.
- [10] Stuart Currie, Nigel Hoggard, Ian J Craven, Marios Hadjivassiliou, and Iain D Wilkinson. “Understanding MRI: basic MR physics for physicians.” In: *Postgraduate medical journal* 89.1050 (2013), pp. 209–23. ISSN: 1469-0756. DOI: 10.1136/postgradmedj-2012-131342. URL: <http://www.ncbi.nlm.nih.gov/pubmed/23223777>.
- [11] Data Spectrum Corporation. *Frequently Asked Questions - How do I eliminate air bubbles in the Mini, Micro and Ultra Micro line of phantoms?* \url{http://www.spect.com/faq.html}
- [12] Marc Debois, Raymond Oyen, Frederik Maes, Geert Verswijvel, Giovanna Gatti, Hilde Bosmans, Michel Feron, Erwin Bellon, Gerald Kutcher, Hein Van Poppe, and Luc Vanuytsel. “The contribution of magnetic resonance imaging to the three-dimensional treatment planning of localized prostate cancer”. In: *International Journal of Radiation Oncology Biology Physics* 45.4 (1999), pp. 857–865. ISSN: 03603016. DOI: 10.1016/S0360-3016(99)00288-6. URL: <http://www.sciencedirect.com/science/article/pii/S0360301699002886>.
- [13] *DICOM: About DICOM.* \url{http://dicom.nema.org/Dicom/about-DICOM.html}. URL: <http://dicom.nema.org/Dicom/about-DICOM.html> (visited on 01/08/2017).
- [14] Jeff H. Duyn. *The future of ultra-high field MRI and fMRI for study of the human brain.* 2012. DOI: 10.1016/j.neuroimage.2011.10.065. arXiv: NIHMS150003.
- [15] Judith Enders, Elke Zimmermann, Matthias Rief, Peter Martus, Randolph Klingebiel, Patrick Asbach, Christian Klessen, Gerd Diederichs, Moritz Wagner, Ulf Teichgr??ber, Thomas Bengner, Bernd Hamm, and Marc Dewey. *Reduction of claustrophobia with short-bore versus open magnetic resonance imaging: A randomized controlled trial.* 2011. DOI: 10.1371/journal.pone.0023494.
- [16] Alice R. Goldman and Pierre D. Maldjian. *Reducing radiation dose in body CT: A practical approach to optimizing CT protocols.* 2013. DOI: 10.2214/AJR.12.10330.

- [17] Peter Greer, D Ph, Jason Dowling, D Ph, Peter Pichler, Jidi Sun, M Sc, Haylea Richardson, B Med Rad Sc, David Rivest-henault, D Ph, Soumya Ghose, D Ph, Jarad Martin, Chris Wratten, Jameen Arm, Leah Best, Jim Denham, and Peter Lau. “Development of MR-only Planning for Prostate Radiation Therapy Using Synthetic CT”. In: (2015), pp. 61–62.
- [18] Alexandra Hellerbach, Verena Schuster, Andreas Jansen, and Jens Sommer. “MRI Phantoms – Are There Alternatives to Agar?” In: *PLoS ONE* 8.8 (2013). DOI: 10.1371/.
- [19] William Henry. “Experiments on the Quantity of Gases Absorbed by Water, at Different Temperatures, and under Different Pressures”. In: *Philosophical Transactions of the Royal Society of London* 93.1 (1803), pp. 29–274. ISSN: 02610523. DOI: 10.1098/rstl.1803.0004. URL: http://www.jstor.org/stable/107068?seq=1{\#}page{_}scan{_}tab{_}contents.
- [20] J. D. Hunter. *Matplotlib: A 2D graphics environment*. \url{http://matplotlib.org/}. 2007. DOI: 10.1109/MCSE.2007.55.
- [21] Edward F Jackson. “MR Acceptance Testing and Quality Control : Previous MR Committee TG Reports MRI Acceptance Testing - E . Jackson Levels of Involvement MR Acceptance Test Reality Check MR Siting Issues”. In: 17.1 (2009), pp. 287–295.
- [22] Edward F. Jackson, Michael J. Bronskill, Dick J. Drost, Joseph Och, Wlad T. Sobol, and Geoffrey D. Clarke. *AAPM Report No. 100 Acceptance Testing and Quality Assurance Procedures for Magnetic Resonance Imaging Facilities Report of MR Subcommittee Task Group I*. 100. 2010, pp. 1–32. ISBN: 9781936366026.
- [23] R Kikinis. *Overview: functions of 3D Slicer*. \url{http://perk.cs.queensu.ca/sites/perk.cs.quee 04-30-Kikinis-Slicer-reduced.pdf}. 2012.
- [24] Adamos Kyriakou. *DICOM in Python: Importing medical image data into NumPy with PyDICOM and VTK*. \url{https://pyscience.wordpress.com/2014/09/08/dicom-in-python-importing-medical-image-data-into-numpy-with-pydicom-and-vtk/}. (Visited on 01/10/2017).
- [25] Adamos Kyriakou. *Image Segmentation with Python and SimpleITK*. \url{https://pyscience.w segmentation-with-python-and-simpleitk/}.

- [26] Tuong Le. “High-field, high-performance magnetic resonance: Technical challenges and clinical applications”. In: *The journal of practical medical imaging and management* (2004), pp. 1–8.
- [27] A.D.A Maidment and M.J Yaffe. “Mammography”. In: *Diagnostic Radiology Physics A Handbook for Teachers and Students* (2014), pp. 209–235.
- [28] R Mathur-De Vre, R Grimee, F Parmentier, and J Binet. “The use of agar gel as a basic reference material for calibrating relaxation times and imaging parameters.” In: *Magnetic resonance in medicine : official journal of the Society of Magnetic Resonance in Medicine / Society of Magnetic Resonance in Medicine* 2.2 (1985), pp. 176–179. ISSN: 0740-3194. DOI: 10.1002/mrm.1910020208.
- [29] Cynthia H. McCollough, Andrew N. Primak, Natalie Braun, James Kofler, Lifeng Yu, and Jodie Christner. *Strategies for Reducing Radiation Dose in CT*. 2009. DOI: 10.1016/j.rcl.2008.10.006.
- [30] *MedPy 0.2.2 : Python Package Index*. \url{https://pypi.python.org/pypi/MedPy}. URL: <https://pypi.python.org/pypi/MedPy> (visited on 12/19/2016).
- [31] *medpy.metric.binary — MedPy 0.2.2 documentation*. \url{http://pythonhosted.org/MedPy/_modul... URL: http://pythonhosted.org/MedPy/_modules/medpy/metric/binary.html (visited on 12/19/2016).
- [32] *medpy.metric.binary.dc — MedPy 0.2.2 documentation*. \url{http://pythonhosted.org/MedPy/gener... URL: <http://pythonhosted.org/MedPy/generated/medpy.metric.binary.dc.html> (visited on 12/19/2016).
- [33] Takashi Mizowaki, Yasushi Nagata, Kaoru Okajima, Masaki Kokubo, Yoshiharu Negoro, Norio Araki, and Masahiro Hiraoka. “Reproducibility of geometric distortion in magnetic resonance imaging based on phantom studies”. In: *Radiotherapy and Oncology* 57.2 (2000), pp. 237–242. ISSN: 01678140. DOI: 10.1016/S0167-8140(00)00234-6.
- [34] Martin J Murphy, James Balter, Stephen Balter, Jose a BenComo, Indra J Das, Steve B Jiang, C M Ma, Gustavo H Olivera, Raymond F Rodebaugh, Kenneth J Ruchala, Hiroki Shirato, and Fang-Fang Yin. “The management of imaging dose during image-guided radiotherapy: report of the AAPM Task Group 75.” In: *Medical physics* 34.10 (2007), pp. 4041–4063. ISSN: 00942405. DOI: 10.1118/1.2775667.

- [35] K Nakamura, E T Al., and (Particle Data Group). “Passage of particles through matter”. In: *Journal of Physics* G.37 (2010), p. 075021. ISSN: 1434-6044. DOI: and2011partialupdateforthe2012edition.(pdg.lbl.gov).
- [36] Tufve Nyholm and Joakim Jonsson. “Technical Aspects of MR-only Radiotherapy”. In: (2015), pp. 65–67.
- [37] Joseph G Och, Geoffrey D Clarke, Wladyslaw T Sobol, Coleman W Rosen Seong, Ki Mun, Coleman W Rosen, and Seong Ki Mun. “ACCEPTANCE TESTING OF MAGNETIC RESONANCE IMAGING SYSTEMS* Acceptance testing of magnetic resonance imaging systems: Report of AAPM Nuclear Magnetic Resonance Task Group No. 6 a”. In: *Reprinted from MEDICAL PHYSICS* 19.1 (1992), pp. 271–7344. ISSN: 0094-2405. DOI: 10.1118/1.596903.
- [38] Harald Paganetti and Thomas Bortfeld. *Proton beam radiotherapy - The state of the art*. October. 2005, pp. 3–540. ISBN: 3540003215. DOI: 10.1118/1.1999671. URL: <http://www.aapm.org/meetings/05AM/pdf/18-4016-65735-22.pdf>.
- [39] Bernhard Petersch, Joachim Bogner, Annette Fransson, Thomas Lorang, and Richard Pötter. “Effects of geometric distortion in 0.2 T MRI on radiotherapy treatment planning of prostate cancer”. In: *Radiotherapy and Oncology* 71.1 (2004), pp. 55–64. ISSN: 01678140. DOI: 10.1016/j.radonc.2003.12.012.
- [40] “Physico-Chemical Properties”. In: () .
- [41] E B Podgorsak. “Radiation Oncology”. In: *Radiation Oncology* () .
- [42] Ryan G. Price, Mo Kadbi, Joshua Kim, James Balter, Indrin J. Chetty, and Carri K. Glide-Hurst. “Technical Note: Characterization and correction of gradient non-linearity induced distortion on a 1.0 T open bore MR-SIM”. In: *Medical Physics* 42.10 (2015), pp. 5955–5960. ISSN: 0094-2405. DOI: 10.1118/1.4930245. URL: <http://scitation.aip.org/content/aapm/journal/medphys/42/10/10.1118/1.4930245>.
- [43] *Pydicom*. \url{http://pydicom.readthedocs.io/en/stable/getting_started.html}. (Visited on 01/10/2017).
- [44] *Python 2.7.13*. \url{https://www.python.org/}. (Visited on 01/10/2017).

- [45] Christopher M. Rank, Nora Hünemohr, Armin M. Nagel, Matthias C. Röthke, Oliver Jäkel, and Steffen Greilich. “MRI-based simulation of treatment plans for ion radiotherapy in the brain region”. In: *Radiotherapy and Oncology* 109.3 (2013), pp. 414–418. ISSN: 01678140. DOI: 10.1016/j.radonc.2013.10.034.
- [46] Coen Rasch, Isabelle Barillot, Peter Remeijer, Adriaan Touw, Marcel Van Herk, and Joos V. Lebesque. “Definition of the prostate in CT and MRI: A multi-observer study”. In: *International Journal of Radiation Oncology Biology Physics* 43.1 (1999), pp. 57–66. ISSN: 03603016. DOI: 10.1016/S0360-3016(98)00351-4.
- [47] Mack Roach, Pamela Faillace-Akazawa, Christine Malfatti, John Holland, and Hedvig Hricak. “Prostate volumes defined by magnetic resonance imaging and computerized tomographic scans for three-dimensional conformal radiotherapy”. In: *International Journal of Radiation Oncology Biology Physics* 35.5 (1996), pp. 1011–1018. ISSN: 03603016. DOI: 10.1016/0360-3016(96)00232-5.
- [48] Martin Rohrer, Hans Bauer, Jan Mintorovitch, Martin Requardt, and Hanns-Joachim Weinmann. “Comparison of Magnetic Properties of MRI Contrast Media Solutions at Different Magnetic Field Strengths”. In: () .
- [49] B K Rutt and D H Lee. “The impact of field strength on image quality in MRI.” In: *Journal of magnetic resonance imaging : JMRI* 6.1 (1996), pp. 57–62. ISSN: 1053-1807. DOI: 3TLibrary-Converted#12;Usedtobe#1642.
- [50] R. Sander. “Compilation of Henry’s law constants (version 4.0) for water as solvent”. In: *Atmospheric Chemistry and Physics* 15.8 (2015), pp. 4399–4981. ISSN: 16807324. DOI: 10.5194/acp-15-4399-2015.
- [51] U Schneider, E. Pedroni, and Antony Lomax. “The calibration of CT Hounsfield units for radiotherapy treatment planning.” In: *Physics in medicine and biology* 41.1 (1996), pp. 111–24. ISSN: 0031-9155. DOI: 10.1088/0031-9155/41/1/009. arXiv: arXiv:1011.1669v3. URL: <http://www.ncbi.nlm.nih.gov/pubmed/8685250>.
- [52] *SimpleITK*. \url{http://www.simpleitk.org/}. (Visited on 12/19/2016).
- [53] *SimpleITK: IPython Notebooks*. \url{http://insightsoftwareconsortium.github.io/SimpleITK-Notebooks/}. (Visited on 12/19/2016).
- [54] *SimpleITK/GettingStarted - KitwarePublic*. \url{https://itk.org/Wiki/SimpleITK/GettingStarted}. URL: <https://itk.org/Wiki/SimpleITK/GettingStarted> (visited on 01/10/2017).

- [55] A. B. Smith, W. P. Dillon, R. Gould, and Max Wintermark. *Radiation dose-reduction strategies for neuroradiology CT protocols*. 2007. DOI: 10.3174/ajnr.A0814.
- [56] Aaron Sodickson, Pieter F Baeyens, Katherine P Andriole, Luciano M Prevedello, Richard D Nawfel, Richard Hanson, and Ramin Khorasani. “Recurrent CT, cumulative radiation exposure, and associated radiation-induced cancer risks from CT of adults.” In: *Radiology* 251.1 (2009), pp. 175–184. ISSN: 0033-8419. DOI: 10.1148/radiol.2511081296. URL: <http://pubs.rsna.org/doi/abs/10.1148/radiol.2511081296>.
- [57] Teodor Stanescu, Jans Hans-Sonke, Pavel Stavrev, and B. Gino Fallone. “3T MR-based treatment planning for radiotherapy of brain lesions”. In: *Radiology and Oncology* 40.2 (2006), pp. 125–132. ISSN: 13182099. URL: <http://www.scopus.com/inward/record.url?eid=2-s2.0-33746661222&partnerID=tZ0tx3y1>.
- [58] Tarraf Torfeh, Rabih Hammoud, Maeve McGarry, Noora Al-Hammadi, and Gregory Perkins. “Development and validation of a novel large field of view phantom and a software module for the quality assurance of geometric distortion in magnetic resonance imaging.” In: *Magnetic Resonance Imaging* 33.7 (2015), pp. 939–949. ISSN: 0730725X. DOI: 10.1016/j.mri.2015.04.003. URL: <http://eutils.ncbi.nlm.nih.gov/entrez/eutils/elink.fcgi?dbfrom=pubmed&id=25882440&retmode=ref&cmd=prlinks%5Cnpapers3://publication/doi/10.1016/j.mri.2015.04.003http://eutils.ncbi.nlm.nih.gov/entrez/eutils/elink.fcgi?dbfrom=pubmed%7B&%7D&id=25882440%7B&%7D&retmode=re>.
- [59] Bernard E. Van Beers, Catherine M. Pastor, and Hero K. Hussain. *Primovist, eovist: What to expect?* 2012. DOI: 10.1016/j.jhep.2012.01.031.
- [60] Hitoshi Wada, Masaki Sekino, Hiroyuki Ohsaki, Tatsuhiro Hisatsune, Hiroo Ikehira, and Tsukasa Kiyoshi. “Prospect of high-field MRI”. In: *IEEE Transactions on Applied Superconductivity*. Vol. 20. 3. 2010, pp. 115–122. ISBN: 1051-8223. DOI: 10.1109/TASC.2010.2043939.
- [61] Amy Walker, Gary Liney, Lois Holloway, Jason Dowling, David Rivest-Henault, and Peter Metcalfe. “Continuous table acquisition MRI for radiotherapy treatment planning: Distortion assessment with a new extended 3D volumetric phantom.” In:

Medical physics 42.4 (2015), p. 1982. ISSN: 0094-2405. DOI: 10.1118/1.4915920.
URL: <http://www.ncbi.nlm.nih.gov/pubmed/25832089>.

- [62] Deming Wang, David M. Doddrell, and Gary Cowin. “A novel phantom and method for comprehensive 3-dimensional measurement and correction of geometric distortion in magnetic resonance imaging”. In: *Magnetic Resonance Imaging* 22.4 (2004), pp. 529–542. ISSN: 0730725X. DOI: 10.1016/j.mri.2004.01.008.
- [63] Deming Wang, Wendy Strugnell, Gary Cowin, David M. Doddrell, and Richard Slaughter. “Geometric distortion in clinical MRI systems: Part II: Correction using a 3D phantom”. In: *Magnetic Resonance Imaging* 22.9 (2004), pp. 1223–1232. ISSN: 0730725X. DOI: 10.1016/j.mri.2004.08.014.